EUROFUSION WP15ER-PR(16) 16394

S Briguglio et al.

Saturation of Alfven modes in Tokamak plasmas investigated by Hamiltonian mapping techniques

Preprint of Paper to be submitted for publication in
Nuclear Fusion

This work has been carried out within the framework of the EUROfusion Consortium and has received funding from the Euratom research and training programme 2014-2018 under grant agreement No 633053. The views and opinions expressed herein do not necessarily reflect those of the European Commission.

Saturation of Alfvén modes in Tokamak plasmas investigated by Hamiltonian mapping techniques

S. Briguglio[1], M. Schneller[2], X. Wang[3], T. Hayward[3],

V. Fusco[1], C. Di Troia[1], G. Vlad[1] and G. Fogaccia[1]

1. Associazione Euratom-ENEA sulla Fusione, C.P. 65 - I-00044 - Frascati, Italy

2. Princeton Plasma Physics Laboratory, Princeton, NJ 08543, USA

3. Max Planck Institute for Plasma Physics, 85748 Garching, Germany

Abstract

Nonlinear dynamics of single toroidal number gap Alfvén modes destabilised by the the resonant interaction with fast ions is investigated, in Tokamak equilibria, by means of Hamiltonian mapping techniques. The results obtained by two different simulation codes, XHMGC and HAGIS, are considered with reference to $n = 2$ Beta induced Alfvén Eigenmodes and, respectively $n = 6$ Toroidal Alfvén Eigenmodes; simulations of the bump-on-tail instability performed by a 1-dimensional code, PIC1DP, are also analysed. A general feature emerges from these results: modes saturate as the resonant-particle distribution function is flattened, because of the fluxes associated to the motion of particles captured in the potential well of the wave, over the whole region where mode-particle power transfer can take place in the linear phase. Such region can be limited by the narrowest of the resonance width and the mode width. In the former case, mode amplitude at saturation exhibits a quadratic scaling with the linear growth rate; in the latter case, a linear growth rate. These findings are explained in terms of the approximate analytic solution of a nonlinear pendulum model. They are also used to prove that the radial width of the single poloidal harmonic sets an upper limit to the radial displacement of passing fast ions produced by a single-toroidal-number gap mode in the large n limit, irrespectively of the possible existence of a large global mode structure formed by many harmonics.

I. INTRODUCTION

In Tokamak plasmas, Alfvén modes can be driven unstable by the resonant interaction with fast particles, like alpha particles produced by fusion reactions and/or fast ions produced by auxiliary heating methods, as such particles are characterised by speeds of the order of the Alfvén velocity. The nonlinear interaction with Alfvén modes can in turn degradate the confinement of these ions, preventing their thermalisation in the core plasma and possibly damaging the first wall. The relevance of this phenomenon depends on the details of the nonlinear dynamics of the modes: how large is the fraction of fast ions involved, the amplitude at which modes saturate, the fast-ion radial displacement under the action of the modes. The capability of predicting the linear stability of proposed scenarios with respect to Alfvén modes and the nonlinear effects on fast-ion dynamics in the presence of growing modes is then an important element in the route towards the realisation of a nuclear fusion reactor (or, more immediately, a burning plasma experiment).

A large effort has been devoted to the linear stability analysis of tokamak plasmas in the presence of fast-ion minorities[1–6]. It has been shown that Alfvén modes can exist in the gaps formed, in the Alfvén continuum, by toroidicity, ellipticity and other equilibrium effects, as well as finite bulk-plasma β effects (with β being the ratio between kinetic and magnetic pressure). These modes, called Toroidal Alfvén Eigenmodes (TAEs), Ellipticity-induced Alfvén Eigenmodes (EAEs), Beta-induced Alfvén Eigenmodes (BAEs), etc., are quasi-marginally stable magnetohydrodynamic (MHD) modes, easily driven unstable in the presence of fast ions. Besides gap modes, continuum oscillation, strongly damped in the MHD limit (no fast-ion contribution), can be destabilised by the resonant interaction with fast ions, provided that the pressure gradient of such ions exceeds a certain threshold. These latter modes have been dubbed Energetic Particle Modes[7] (EPMs).

The nonlinear dynamics of Alfvén modes has been deeply analysed in certain limits. In particular, the very weak-mode limit has been thoroughly studied by Berk and Breizman[8–10]. In this limit the problem can be reduced to a one-dimensional (1D) problem, and the Alfvén mode dynamics can be treated as that of the bumb-on-tail instability[11–14]. Mode saturate via the flattening of fast-ion distribution function (that is, the reduction of the free-energy source for instability). Saturation is reached as the flattening extends over the whole phase-space region where the resonance condition is satisified (that is, where the

particle resonance frequency differs from the mode frequency by an amount not much larger than the mode growth rate). This condition yields a quadratic dependence of the saturation mode amplitude on the linear growth rate. In this near-marginal stability regime, the radial excursion of fast ions due to the mode-particle interaction is so limited that it does not allow resonant particles to perceive any of the (equilibrium or fluctuation induced) non-uniformities characterising the system.

The other limit examined in literature is that of strongly unstable EPMs. Both numerical and analytic works [15, 16] have shown that these modes saturate because a macroscopic distortion of the whole fast-ion pressure profile, accompanied by a significant variation of mode frequency and spatial structure. It has been shown [16] that this mechanism can give rise to avalanches, with an outwardly moving front of pressure gradient: shear-Alfvén continuum oscillations are driven progressively unstable by the radially drifting free energy source. In this non-perturbative, strongly-driven regime, the radial excursion of resonant particles is so essential that it self-consistently determines the nonlinear mode structure evolution. This phenomenon has been described in terms of the so-called "fishbone paradigm"[17, 18], reminding the dynamics associated to bursting ejection of fast ions, observed in the Poloidal Divertor eXperiment (PDX) tokamak[19, 20].

Intermediate regimes have been examined by numerical simulation studies[21–24]. Several points have been evidenced. On one side, it has been shown that modes characterised by different toroidal numbers can cooperate in affecting fast ion transport[22]. Second, the nonlinear modification of mode frequency (so-called frequency chirping) and structure has been observed even for very weak (slightly above threshold) EPMs[23]. Finally, the relevance of finite mode structure in determining the saturation process of gap modes has been pointed out[21], and the transition from the quadratic scaling to a weaker one, for the saturation mode amplitude, as the growth rate increases above a certain level has been demonstrated[24].

In the present paper, we will consider only the latter phenomenon. It is characterised, even during the nonlinear evolution of the mode, by constant frequency. To simplify the analysis, we will analyse the evolution of a mode characterised by a single toroidal number n. Under these conditions (constant frequency and single toroidal number), resonant particle behaviour can be analysed by Hamiltonian mapping techniques[21, 25].

Aim of our paper is investigating whether the saturation dynamics presents quite general

features. To overcome the unsatisfactory character of a numerical analysis (apparently limited to a certain numerical tool and to the specific problem analysed), we compare the results obtained by different codes, each applied to a different problem. In particular, we present the results obtained by two 3D codes: XHMGC[15, 26, 27] and HAGIS[28]; and a simple δf Vlasov-Poisson 1D code, PIC1D-PETSc[29, 30] (indicated, in the following, as PIC1DP).

We show that the quadratic growth-rate scaling for the saturation amplitude is obtained by all the codes in the limit in which mode-particle resonant interactions are not able to feel the finite structure of the mode along the relevant coordinate (that is, the coordinate along which the distribution function gradient plays the role of free-energy source for instability) during the whole nonlinear evolution of the mode. As soon such finite structure is appreciated by resonant particles (this is possible only for the 3D codes, for not too weak modes), a transition a linear scaling is observed. In this latter regime, the flattening of fast-ion distribution function is limited, at saturation, by the width of the mode, rather than the width of the resonance region.

These results are interpreted on the basis of a simple nonlinear-pendulum model. It is shown that it yields analogous results as the three, more complex, simulation codes considered. An approximate analytic solution is obtained for the model and it is used to predict the behaviour of the simulation codes. The agreement of such predictions with the detailed behaviour of these codes is satisfactory, and it allows us for interpreting the scaling observed for the saturation mode amplitude.

Finally, the relationship linking the width of the distribution-function flattening to resonance and mode width is used to predict the influence of single (and large) toroidal number gap modes (in particular, TAEs) on the radial redistribution of resonant fast ions (in particular, passing ions).

The paper is structured as follows. Section II describes the numerical codes considered in the present paper and presents the Hamiltonian mapping analysis interfaced with such codes. The different cases investigated by each code and the relative results are exposed in Sect. III. The nonlinear pendulum model, developed to interpret these results, is treated in Sect. IV. Predictions based on the approximate analytical solution of the model are compared with the effective results obtained by the different codes in Sect. V. Section VI estimates from these results the upper limit to the radial displacement expected, for passing fast ions,

in presence of large-n BAEs, TAEs or EAEs. Summary and conclusions are presented in Sect. VII.

II. NUMERICAL SIMULATION TOOLS

In this Section, the different numerical particle-in-cell (PIC) codes considered in this paper are described, along with a diagnostic tool, based on Hamiltonian mapping analysis, suited for the particular limit examined in the paper (namely, the evolution of a single toroidal number mode characterised by essentially constant frequency).

A. XHMGC

The code XHMGC, developed at the Frascati laboratories, is the extended version [27] of the HMGC [15, 26], a nonlinear code based on the hybrid MHD gyrokinetic model [31]. The code has been used to investigate fast-ion driven modes (such as TAEs, BAEs and EPMs [15, 24, 32, 33]), as well as to analyse modes observed in existing devices (JT-60U [34], DIII-D [35]) or expected in forthcoming burning plasmas (ITER [36, 37]) and proposed experiments (FAST [38–40]). The fluid response of the thermal background plasma is described by a set of $O(\epsilon^3)$-reduced MHD equations [41] (with ϵ being the inverse aspect ratio) for a low-β plasma, and the fast-ion and thermal-ion kinetic dynamics enter via the respective pressure tensors, which are computed by solving the Vlasov equation for each species in the drift-kinetic limit by PIC techniques. Finite-Larmor-radius effects are ignored, while finite-orbit widths are taken into account in order to retain resonant wave-particle dynamics associated with the drifts induced by curvature and non-homogeneity of the equilibrium magnetic field in toroidal geometry [42, 43]. Assuming cold electrons, ideal-MHD Ohm's law ($E_\parallel = 0$) could be considered; XHMGC requires, however, a small resistivity, for numerical-stability reasons. Kinetic contributions are treated in a non perturbative way: pressure-tensor terms contribute to determine both structure and evolution of electromagnetic fields.

B. HAGIS

The code HAGIS [28] has been developed in the framework of a joint project carried on by Culham and Max Planck Institute for Plasma Physics groups. It evolves the phase-space coordinates of a fast-ion population in the drift kinetic limit, in the presence of electromagnetic modes. For each toroidal number, mode structure and linear frequency are pre-calculated, in realistic magnetic equilibria, by the linear gyrokinetic, electromagnetic code LIGKA [44], which takes into account both bulk-plasma and fast-ion kinetic effects. Such elements are kept fixed, along with a prescribed amount of damping, during HAGIS simulations. Modes' growth rates are instead computed, at each time step, in terms of the instantaneous power exchange between modes and fast ions; frequency perturbations can also be computed on the same basis. Fast ion nonlinearities are fully retained, while fluid mode-mode couplings are neglected. Among other applications, HAGIS has been used to study MAST observations [45], understand energetic particle losses observed in ASDEX Upgrade [46] and predict fast-ion behaviour in ITER [5, 22].

C. PIC1DP

PIC1DP [29, 30] is a δf PIC code simulating 1D electrostatic plasma by solving the Vlasov-Poisson equation system. It upgrades an original 1D code, PIC1D [47] by recasting the PIC approach in a vector-matrix form and adopting PETSc[48], a suite of data structures and routines, for the parallel implementation of the code.

The 1D Vlasov-Poisson system can be written as

$$\frac{\partial f_j}{\partial t} + v\frac{\partial f_j}{\partial x} - \frac{q_j}{m_j}\frac{\partial \varphi}{\partial x}\frac{\partial f_j}{\partial v} = 0 \tag{1}$$

$$\frac{\partial^2 \varphi}{\partial x^2}(x,t) = -4\pi \sum_{j=e,i} q_j n_j(x,t) \tag{2}$$

$$n_j(x,t) \equiv \int_{-\infty}^{\infty} f_j(x,v,t)dv \tag{3}$$

$$\tag{4}$$

where f_j, q_j, m_j and n_j are, respectively, distribution function, charge, mass and density of the j species (electrons or ions), and φ is the electrostatic potential. In our simulations, we will treat ions as a static background, solving the Vlasov equation only for electrons.

D. Hamiltonian mapping analysis

Limiting our analysis to single toroidal mode number (n), constant frequency (ω) modes allows us to take advantage from the existence of two constants of the perturbed particle motion of the fast ("Hot") ions. Indeed, besides the magnetic momentum $M \equiv m_H v_\perp^2/2\Omega_H$, the quantity $C \equiv \omega P_\phi - nE$, with P_ϕ being the toroidal angular momentum and $E \equiv m_H U^2/2 + M\Omega_H$ the fast-ion kinetic energy, is conserved, as it can be easily recovered from the equations of motion in the Hamiltonian form [25],

$$dP_\phi/dt = -\partial H/\partial\phi \tag{5}$$

and

$$dE/dt = \partial H/\partial t, \tag{6}$$

where H is the single particle Hamiltonian, characterised by time and toroidal angle (ϕ) dependence in the form $H = H(\omega t - n\phi)$. In the previous expressions, $v_\perp$ is the magnitude of particle velocity perpendicular to the equilibrium magnetic field, $\Omega_H = e_H B/m_H c$ is the cyclotron frequency, m_H and e_H are fast-ion mass and charge, respectively, B is the magnitude of local equilibrium magnetic field, U is the parallel (to the equilibrium magnetic field) velocity and c is the speed of light. At the leading order, we can approximate

$$P_\phi \simeq m_H R U + e_H R_0(\psi_{\rm eq} - \psi_{\rm eq0})/c \equiv P_\phi(r, \theta, U) \tag{7}$$

and

$$C \simeq \omega P_\phi - n(m_H U^2/2 + M\Omega_H) \equiv C(r, \theta, M, U), \tag{8}$$

with R being the major-radius coordinate and $\psi_{\rm eq}$ the equilibrium poloidal flux defined by the following expression for the equilibrium magnetic field $\mathbf{B}_{\rm eq} \equiv R_0 B_{\phi 0}\nabla\phi + R_0\nabla\psi_{\rm eq} \times \nabla\phi$, and the label "0" indicating on-axis quantities. Then, cutting the phase space into slices orthogonal to the axes M and C, particles belonging to a certain slice will never leave it; stating this in a different way: gradients of the distribution function in M or C directions neither represent free energy sources for driving the mode unstable, nor evolve in time. Mode-particle power exchange can then be described as the sum of different-slice contributions, each of them evolving in an independent way. Focusing on the most relevant slice (that hosting the maximum power exchange), centred around ($M = M_0, C = C_0$), we can get a deeper insight in the mode-particle interaction. To this aim, the phase-space

slice is sampled by a set of test particles, evolving in the perturbed fields computed by the self-consistent simulation. Each test particle can be represented by a marker in the (Θ, P_ϕ) plane (with Θ being the wave phase seen by the particle). Test-particle coordinates are collected every time ($t = t_j$) the particle crosses the equatorial plane ($\theta = 0$) at its outmost R position. The wave phase at those times is

$$\Theta_j = \omega t_j - n\phi_j + 2\pi j m\sigma, \tag{9}$$

where m is the poloidal mode number and $\sigma \equiv \text{sign}(U)$. The resonance condition is

$$\Delta\Theta_j \equiv \Theta_{j+1} - \Theta_j = 2\pi k, \tag{10}$$

with the integer k denoting the "bounce harmonic". Differentiating Eq. 10 with respect to time, the resonance condition can be written in the form

$$\omega - \omega_{\text{res}}(r, M_0, C_0, k) = 0, \tag{11}$$

with, ω_{res} depending on the relevant resonance condition for the considered phase-space slice. In this paper, we will consider only modes destabilised by the resonant interaction with circulating particles. In such cases,

$$\omega_{\text{res}}(r, M_0, C_0, k) \equiv n\omega_D + [(n\bar{q} - m)\sigma + k]\omega_b. \tag{12}$$

Here [18, 49, 50],

$$\omega_D \equiv \left[\frac{\Delta\phi}{2\pi} - \sigma\bar{q}\right]\omega_b \tag{13}$$

is the precession frequency, $\Delta\phi$ is the change in toroidal angle over the bounce time τ_b (i.e., the time needed to complete a closed orbit in the poloidal plane), defined as

$$\tau_b \equiv \oint \frac{d\theta}{\dot{\theta}}\,, \tag{14}$$

$$\bar{q} \equiv \frac{\sigma}{2\pi}\oint q d\theta\,, \tag{15}$$

with q being the safety factor and the integral taken along the particle orbit; and

$$\omega_b \equiv \frac{2\pi}{\tau_b} \tag{16}$$

is the bounce frequency (in our case, transit frequency). Equation 11 can be solved with respect to r, yielding $r = r_{\text{res}}(\omega, M_0, C_0, k)$, or P_ϕ, yielding $P_\phi = P_{\phi\,\text{res}}(\omega, M_0, C_0, k)$.

In the unperturbed motion, $dP_\phi/dt = 0$. Then, during the linear phase of the mode evolution, the particle trajectories in the (Θ, P_ϕ) plane essentially reduce to fixed points for $P_\phi = P_{\phi\,\mathrm{res}}$, while they correspond to drift along the Θ axis in the positive (negative) direction, for $P_\phi \neq P_{\phi\,\mathrm{res}}$, according to the sign that $\omega - \omega_{\mathrm{res}}$ assumes on each side of $P_{\phi\,\mathrm{res}}$. As the amplitude of the perturbed fields grows, P_ϕ varies because of the mode-particle interaction (e.g., radial $\mathbf{E} \times \mathbf{B}$ drift, with $\mathbf{E}$ being the electric field). Even particles that were initially resonant are brought out of resonance, getting non zero $d\Theta/dt$ and drifting in phase until the field direction and, consequently, the P_ϕ drift are inverted. Particles that cross the $P_\phi = P_{\phi\,\mathrm{res}}$ line invert the sign of $d\Theta/dt$ as well. Thus, their orbits are bounded, and they would properly close them if the field amplitude were constant in time.

The situation we have just described holds for particles born near the resonance. Particles born with P_ϕ far from the resonance maintain, instead, drifting orbits, although perturbed by the interaction with the mode, as they do not cross $P_\phi = P_{\phi\,\mathrm{res}}$. In the following, we will refer to particles that cross $P_\phi = P_{\phi\,\mathrm{res}}$ (and, then, change the sign of $d\Theta/dt$) as particles "captured" by the wave, while defining "trapped" those particles that have completed a full bounce in the wave potential well. As the fluctuating field strength increases, the P_ϕ drift increases and more and more particles are captured and eventually trapped. The formation of these closed-orbit structures, separated from the transit-orbit regions can be seen in Fig. 1. Different frames refer to different times, during the mode evolution for a XHMGC simulation. It is apparent that, in the presence of an equilibrium fast-ion density gradient, the formation of closed orbits correspond to mixing particles originating from the higher-density side of the resonance with particles originating from the lower-density one. It then yields a net outward particle flux and a consequent density flattening around the resonance. Such a flattening involves an increasingly wider region as the mode amplitude increases. At the same time, it causes an increasing reduction of the free energy source for the system instability [21]. In Sect. III we will investigate how this process is related to the mode saturation. Moreover, we will discuss the slight differences required to implement the same method for a 1D system, like that analysed by PIC1DP simulations.

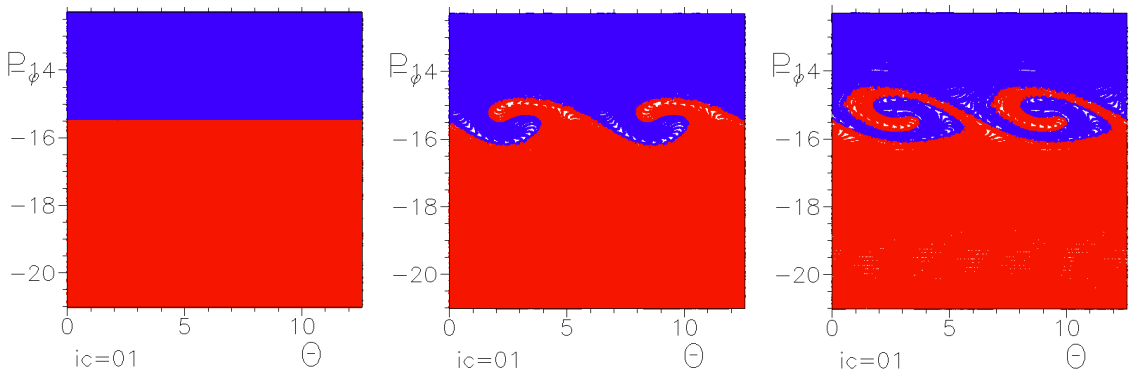

FIG. 1: From left to right: test-particle markers in the (Θ, P_ϕ) plane at three successive times (corresponding to increasing mode amplitude) during the mode evolution in a XHMGC simulation. Each marker is coloured according to the birth P_ϕ value of the particle (red for $P_\phi \leq P_{\phi\,\mathrm{res}}$, blue otherwise). The formation of closed-orbit structures, separated from transit orbits, can be seen in the centre and right frames, corresponding to the nonlinear phase.

III. DIFFERENT CODE RESULTS

In this Section, results of numerical simulations performed by XHMGC, HAGIS and PIC1DP for different cases are presented.

A. XHMGC results

We apply XHMGC to the analysis of a Tokamak equilibrium characterised by shifted circular magnetic surfaces, with aspect ratio $R_0/a = 10$ (a being the minor radius of the torus) and safety factor $q \simeq q_0 + (q_a - q_0)(r/a)^2$, with $q_0 = 1.9$, $q_a = 2.3$ as shown in Fig. 2 (left). Thermal ions are characterised by isotropic Maxwellian initial distribution function with flat density and temperature profiles. The initial distribution function of fast ions (same species as the thermal ones) is instead an anisotropic Maxwellian in the form:

$$F_H \propto \frac{n_H(s)}{T_H^{3/2}} \Xi(\alpha; \alpha_0, \Delta) e^{-E/T_H}. \tag{17}$$

Here, $n_H(s)$, with $s \equiv (1 - \psi_{\rm eq}/\psi_{\rm eq0})^{1/2}$, is the density profile, shown in Fig. 2 (right), $\alpha \equiv \cos^{-1}(U/\sqrt{2E/m_H})$ is the pitch angle. The quantity

$$\Xi(\alpha;\alpha_0,\Delta) \equiv \frac{4}{\Delta\sqrt{\pi}} \frac{\exp\left[-\left(\cos\alpha - \cos\alpha_0\right)^2/\Delta^2\right]}{\mathrm{erf}\left[(1-\cos\alpha_0)/\Delta\right] + \mathrm{erf}\left[(1+\cos\alpha_0)/\Delta\right]} \tag{18}$$

models the anisotropy of the distribution function. Note that, in the isotropic limit ($\Xi = 1$), T_H would assume the meaning of (uniform) temperature. In the present case, we assume an anisotropic initial distribution function characterised by parallel temperature much higher than the perpendicular one, by fixing the width and the peak of the pitch-angle distribution, respectively, as $\Delta = 0.1$ and $\alpha_0 = \cos^{-1}(-1/2)$. We are then essentially dealing with counter-passing fast ions (cf. Fig. 3). Other parameters are $v_H/v_{A0} = 0.3$, $v_i/v_{A0} = 0.06$, $\rho_{H0}/a = 0.01$ and $\rho_{i0}/a = 0.002$, with $\rho_H \equiv v_H/\Omega_H$, $\rho_i \equiv v_i/\Omega_i$, $v_H = (T_H/m_H)^{1/2}$, v_i and Ω_i being, respectively, the bulk-ion thermal velocity and cyclotron frequency, and v_A the Alfvén velocity. Note that the initial distribution function is not a proper equilibrium function, as it is not merely a function of constants of the unperturbed motion. For simplicity, we neglect the consequent initial relaxation of F_H towards a genuine equilibrium, by suppressing the corresponding terms in the evolution of the perturbed distribution function δF_H; this does not affect our results in a significant way, as the typical particle orbit width (which causes ψ not being a constant of the unperturbed motion) is few percent of the minor radius. In the following, for linear simulations, we shall consider a fraction of fast ions, n_{H0}/n_{i0}, ranging in the interval $[0.0014, 0.002]$. Thermal-ion diamagnetic effects are ignored by assuming uniform thermal-ion density and temperature; we instead keep kinetic thermal-ion compressibility effects, in order to include the formation of a kinetic thermal-ion gap. In all the simulations, poloidal harmonics with m from 1 to 6 will be retained. A single toroidal mode number, $n = 2$, is instead retained: this corresponds to neglecting fluid mode-mode coupling in the evolution of electromagnetic fields, while fully taking into account wave-particle nonlinearities.

Figure 4 shows the energy spectrum for the scalar potential, in the (r, ω) plane, for the BAE driven by fast ions with $n_{H0}/n_{i0} = 0.0014$, simulated by XHMGC. The plot refers to the linear-growth phase, but no significant modification is found during the nonlinear phase. It can be seen that the mode is located in the gap opened, in the shear Alfvén continuum, by thermal-ion kinetic effects. For the same case, Fig. 5 reports the radial structure of the different poloidal harmonics, while Fig. 6 shows the power transfer integrated over a

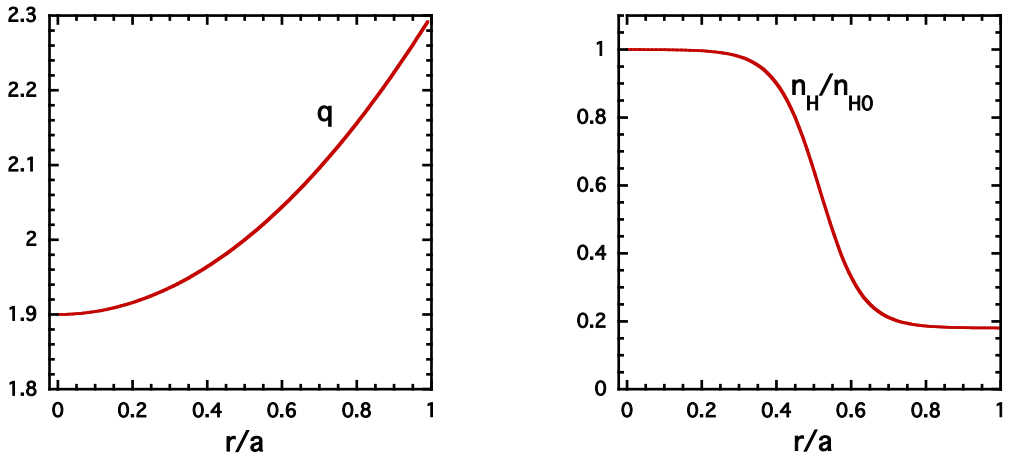

FIG. 2: Radial profiles of safety factor (left) and the $m = 0$ component of the initial fast-ion density normalised to the on-axis value (right), for XHMGC simulations.

toroidal shell around the mode peak, as a function of the velocity-space coordinates (M, U). From such plots we can identify a reduced phase-space point (r_0, M_0, U_0) around which the mode-particle resonant interaction is peaked. From Eq. 8, we can then compute the relative C value as $C_0 = C(r_0, 0, M_0, U_0)$ and select a set of test particles sampling the phase-space slide (M_0, C_0). We fix $r_0/a = 0.5$, $M_0\Omega_{H0}/T_H = 1.25$ and $U_0/v_H = -0.93$, corresponding to $C_0/T_H = -3.89$. With this choice, the relevant bounce harmonic is $k = 1$. Figure 7 compares the mode radial structure, represented by the radial profile of the squared modulus of the perturbed scalar potential integrated over poloidal and toroidal angles, with the resonance structure, represented by the radial profile of the quantity $\gamma/[(\omega - \omega_{\rm res}(r, M_0, C_0, k))^2 + \gamma^2]^{-1/2}$, and the linear-phase power transfer radial structure for such set of resonant test particles. Two cases are considered: the low-drive case $n_{H0}/n_{i0} = 0.0014$ and a larger-drive one, $n_{H0}/n_{i0} = 0.007$. It is immediate to observe two facts: the resonance width increases with the linear growth rate γ; the linear-phase power transfer is radially limited by the narrowest of the resonance structure and the mode one (in fact, for the larger growth rate case, the equilibrium density gradient also plays a role in limiting the power transfer on the inner side).

Figure 1 shows the structures formed by test-particle markers in the (Θ, P_ϕ) plane, for

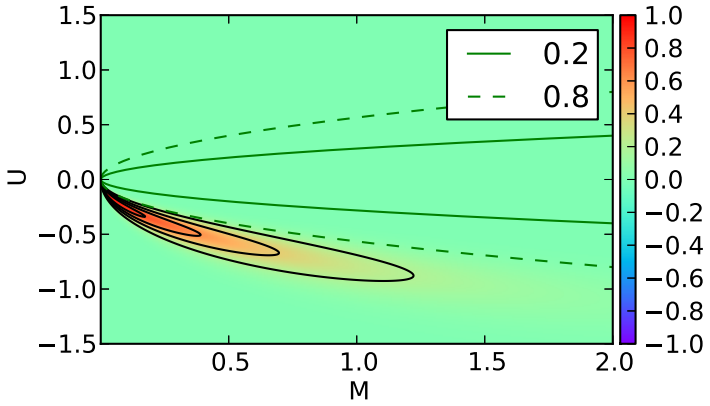

FIG. 3: Contour plot of the initial distribution function in the velocity space for fast ions. Note that M and U are reported in units of T_H/Ω_{H0} and $\sqrt{T_H/m_H}$. Passing-trapped particle boundaries evaluated at the inner ($r/a = 0.2$, solid line) and outer ($r/a = 0.8$, dashed line) limits of the mode's radial domain are shown.

the BAE case considerd in Fig. 4. As pointed out in Sect. II, the formation of $\Theta-$bounded orbits in this plane corresponds to a net particle flux in the P_ϕ direction and a consequent flattening of the resonant-particle density profile. This is shown in Fig. 8, where the test-particle density radial profile is plotted, at saturation, for the two cases considered in Fig. 7. Mode and resonance structures, already shown in Fig. 7, are also reported for comparison. We see that the density flattening at saturation extends over a radial region limited by the resonance condition in the lower growth-rate case; by the mode width, in the larger growth-rate one. This emerges even in a more apparent way, from Fig. 9, which compares, for the BAE XHMGC simulations, the radial widths of mode, resonance and density-flattening region (at saturation), at different values of the linear growth rate. The radial width of the saturation flattening region is limited by the resonance width in the low-γ limit; by the mode width, in the large-γ limit.

Figure 10 reports the saturation amplitude of the scalar potential versus the linear growth rate for the same cases considered in Fig. 9. We see that the transition from the low$-\gamma$ regime (linear power transfer and density flattening limited by the resonance width) to the high$-\gamma$ regime (power transfer and flattening limited by the mode width) mirrors into a corresponding transition from a quadratic γ scaling for the saturation amplitude to a linear

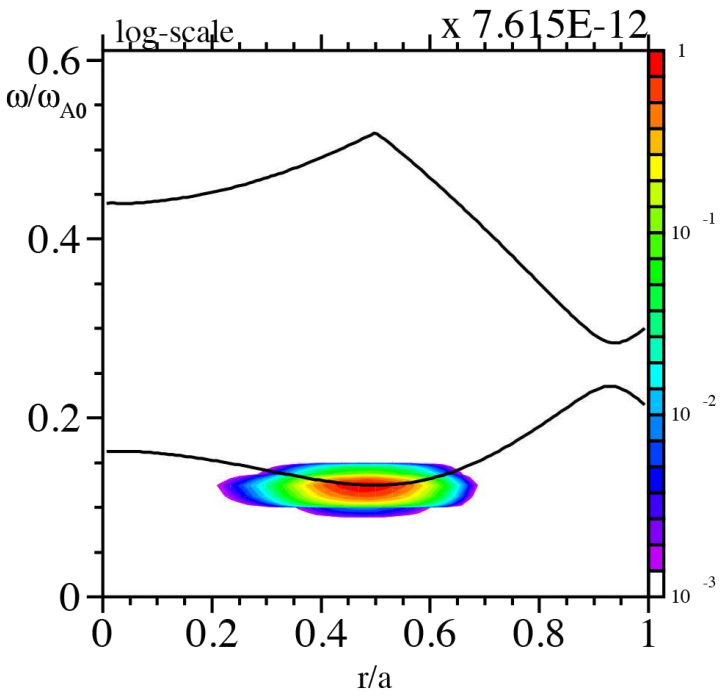

FIG. 4: Energy spectrum for the scalar potential, in the (r, ω) plane, for the BAE driven by fast ions with $n_{H0}/n_{i0} = 0.0014$, simulated by XHMGC. The solid line represents the shear Alfvén continuum with thermal-ion kinetic effects included. The mode is located in the thermal-ion gap.

one. These two regimes have been dubbed, respectively, *resonance detuning* and *radial decoupling*[18, 21].

B. HAGIS results

As far as HAGIS is concerned, here we present results of simulations related to a specific case, connected to the benchmark case [51, 52] carried out in the frame of the International Tokamak Physics Activity (ITPA). Such benchmark, which involved several numerical codes devoted to the investigation of interactions between fast ions and Alfvén modes, was set up with reference to a large aspect ratio circular magnetic surface Tokamak equilibrium ($a = 1$ m, $R_0 = 10$ m), with an equilibrium on-axis toroidal magnetic field $B_0 = 3$T. The

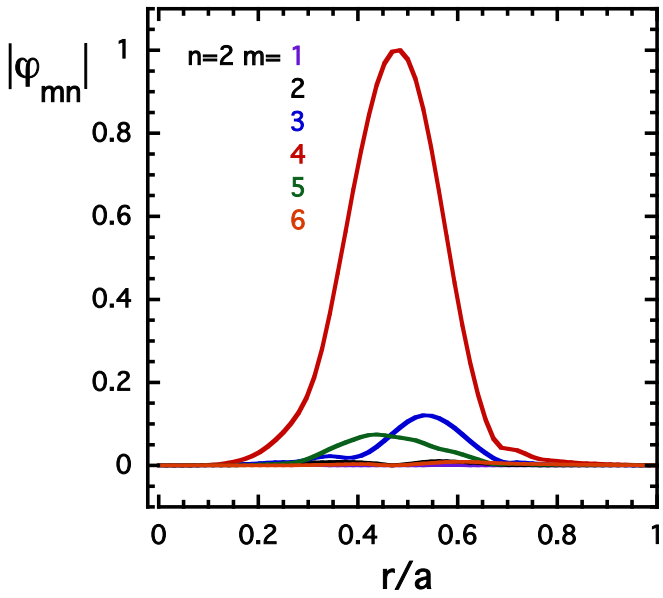

FIG. 5: Radial structure of the modulus of the different poloidal harmonics of the scalar potential, φ_{mn} (with $n = 2$ and m ranging from 1 to 6), for the same case considered in Fig. 4.

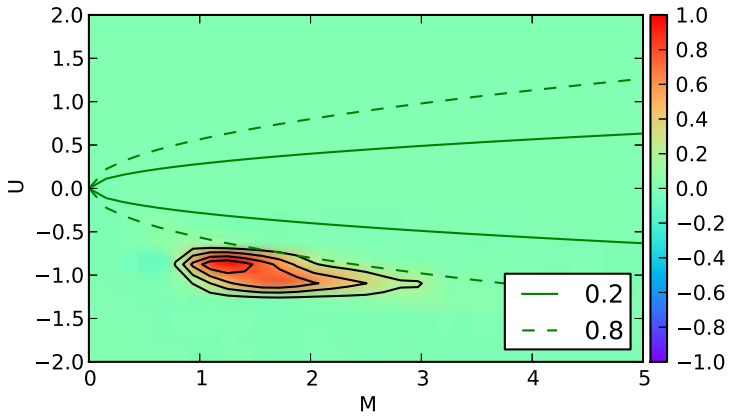

FIG. 6: Power transfer density $P(r, M, U)$, integrated over a toroidal shell centred around the mode peak, for the same case considered in Fig. 4. M and U normalisation are the same as in Fig. 3. Same conventions as in Fig. 3 is also used for dashed and solid lines.

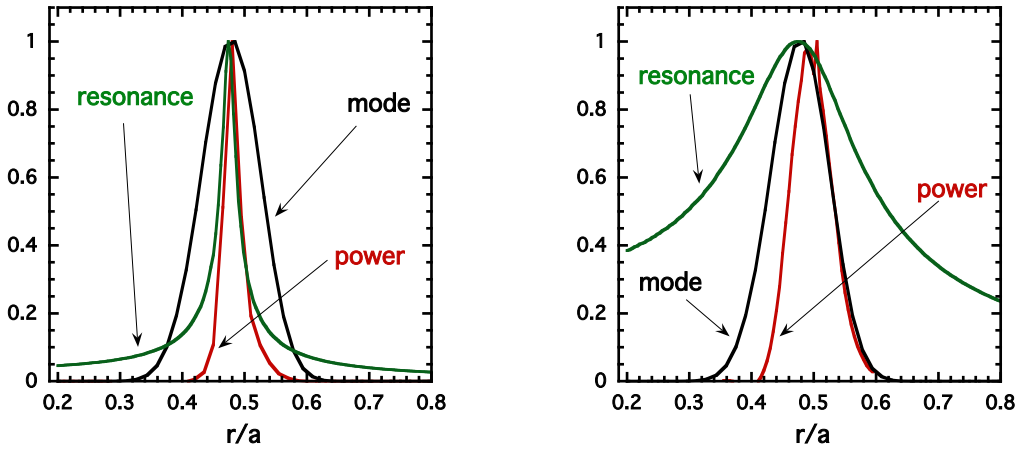

FIG. 7: Resonance radial structure, represented by the radial profile of the quantity $\gamma/[(\omega - \omega_{\rm res}(r, M_0, C_0, k))^2 + \gamma^2]^{-1/2}$ (green curve), compared with the mode structure, represented by the radial profile of the squared modulus of the perturbed scalar potential integrated over poloidal and toroidal angles (black curve), and the effective linear-phase power transfer one (red curve), for the fast-ion selected sets, in the same case considered in Fig. 4. Two different values of the growth rate are considered. The radial extension of power transfer density is limited by the resonance width, for low γ values (left). For large γ values (right), the resonance width does not yield a significant constraint on the power transfer, which is instead limited by mode and density-gradient width (the latter, mainly on the inner side).

bulk plasma pressure profile is given by

$$p(s) = (7.17 \cdot 10^3 - 6.811 \cdot 10^3 s - 3.585 \cdot 10^2 s^2)\ \mathrm{N/m^2}, \tag{19}$$

while the influence of the fast-ion pressure on the magnetic equilibrium is neglected. The resulting safety factor profile is shown in Fig. 11. Uniform density and temperature are assumed for both electrons and bulk ions (hydrogen): $n_{\rm i} = n_{\rm e} = 2.0 \cdot 10^{19}$ m^{-3} and $T_{\rm i} = T_{\rm e} = 1.0$ keV. The initial distribution of fast ions (deuterium) is assumed to be a Maxwellian, with uniform temperature T_H ranging (for the benchmark analysis) from 0 to 800 keV, and

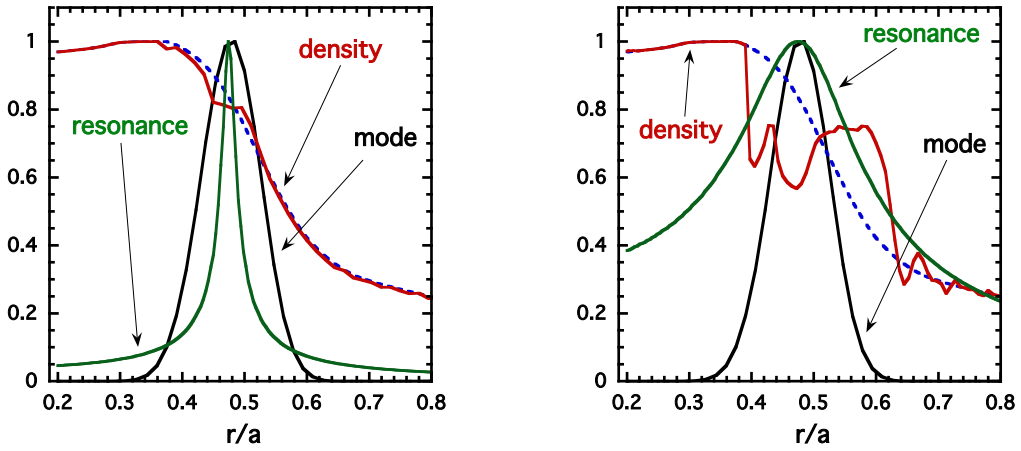

FIG. 8: Test-particle density profile at saturation (red curve) for the test-particle samples compared with the unperturbed one (dashed blue curve), for the same cases considered in Fig. 7. Mode structure is also reported (black curve) along with the resonance structure (green curve). The width of the density flattening region at saturation is limited mainly by the finite resonance width, in the lower growth-rate case (left); by the finite mode width, in the larger growth-rate case (right). Note that in this latter case we use conventionally the expression "flattening" to refer to a strong distortion of the resonant particle density profile.

density profile given by

$$n_H(s) = n_{H0} c_3 \exp\left[-\frac{c_2}{c_1}\tanh\left(\frac{s-c_0}{c_2}\right)\right] \tag{20}$$

with $n_{H0} = 1.44131 \cdot 10^{17}$ m^{-3}, $c_0 = 0.49123$, $c_1 = 0.298228$, $c_2 = 0.198739$, and $c_3 = 0.521298$. In the present paper, we fix $T_H = 400$ keV, while varying n_{H0} from $0.6 \cdot 10^{16}$ to $17.5 \cdot 10^{16}$ m^{-3}. We will neglect finite fast-ion Larmor radius effects, while retaining finite orbit-width effects.

A single toroidal number ($n = 6$) TAE is obtained, for the considered bulk-plasma equilibrium (that is, neglecting the fast-ion contribution), from the code LIGKA, with real frequency $\omega = 0.28\tau_{A0}^{-1}$ (where $\tau_{A0} = R_0/v_{A0}$ is the on-axis Alfvén time). The radial structure of the retained poloidal harmonics (m from 9 to 12) is shown in Fig. 12. The mode amplitude is evolved in time according to the fast-ion response, while its radial structure and real fre-

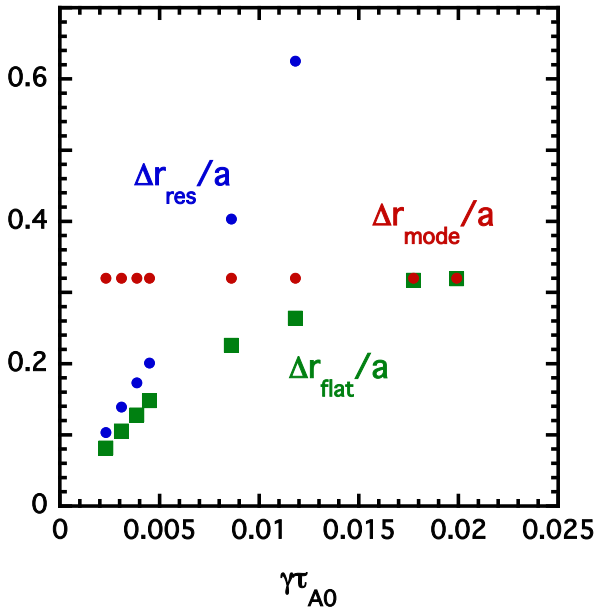

FIG. 9: Radial width of mode (red dots), resonance (blue dots) and density-flattening region at saturation (green squares), at different values of the linear growth rate, for XHMGC simulations. Here, we have conventionally defined the mode width as the width of the region where $|\phi(r)| > 0.05|\phi(r_0)|$; the resonance width, that of the region where $|\gamma/[(\omega - \omega_{\rm res}(r, M_0, C_0, k))^2 + \gamma^2]^{1/2} > 0.2|$. The width of the saturation flattening region is limited by the resonance width in the low-γ limit; by the mode width, in the large-γ limit.

quency are kept fixed. In order to get saturating modes, a time independent damping is included in the amplitude evolution, equal, for each case, to 15% of the linear drive (that is, the linear growth rate obtained in the absence of damping).

Figure 13 shows the contour plot, in the velocity space, for the mode-particle power exchange integrated over a toroidal shell centred around the radial localisation of the mode, for the considered cases. We see that the mode is driven unstable by the transit resonance with co-passing and counter-passing particles. Form this plot we can identify the coordinates (r_0, M_0, U_0) corresponding to the maximum drive and, then, the slice around $M = M_0$ and $C = C_0 \equiv C(r_0, 0, M_0, U_0)$ representative of the relevant resonant-particle dynamics. The

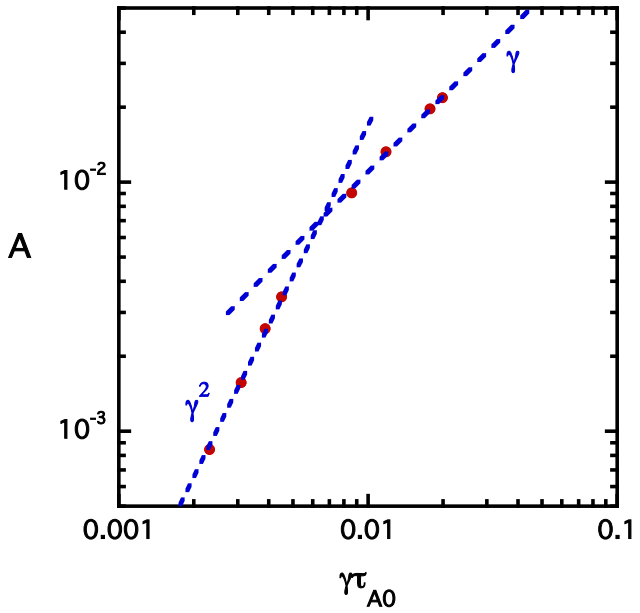

FIG. 10: Scaling of saturation amplitude of scalar potential (defined as the radial peak, in units of T_H/e_H, of the dominant poloidal harmonic) versus the linear growth rate γ for XHMGC simulations. The reference quadratic and linear γ scaling are also shown.

choice adopted for the simulations reported in this paper is $r_0/a = 0.5$, $M_0\Omega_{H0}/T_H = 0.2$ and $U_0/v_H = 1.18$, corresponding to $C_0/T_H = -4.49$

Figure 14, analogous to Fig. 7, compares the radial structure of the power transfer density (in the linear phase) with that of the mode and the radial width of the resonance. As in the XHMGC case, the radial extension of the power transfer region is limited by the resonance width for weak modes; by the mode width, for the stronger modes. Figure 15 shows the formation of closed-orbit structures in the (Θ, P_ϕ) plane, separated from transit orbits, in the nonlinear phase of the simulation considered in Fig. 14. As discussed in Sect. II D, it corresponds to a net outward flux of resonant particles, with a consequent flattening of their density profile. Also in this case, saturation is reached as the density flattening extends over the narrowest of the two relevant regions: that limited by the resonance width, for low growth rate; that limited by the finite mode width, for large growth rate. This is shown in Figs. 16 and 17, while Fig. 18 shows the corresponding transition from quadratic to linear

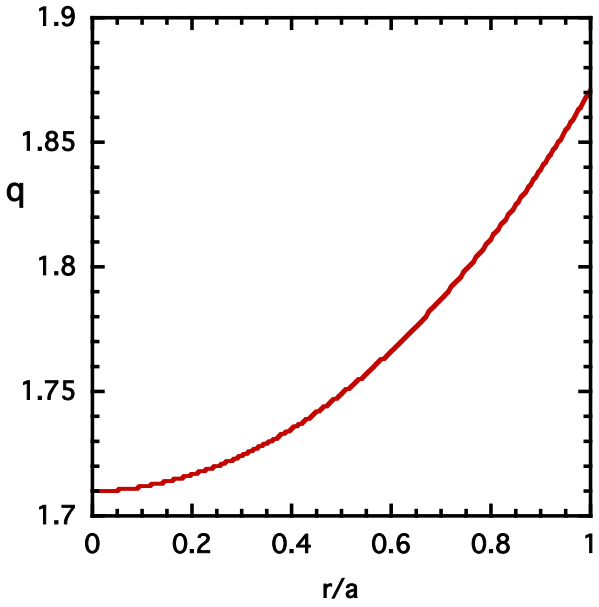

FIG. 11: The q profile for the ITPA benchmark equilibrium. Note that with a so flat profile, there is no significant difference between s and r/a.

γ scaling for the mode saturation amplitude.

C. PIC1DP results

The code PIC1DP is applied here to a simulation of the bump-on-tail instability. The initial distribution function for a homogeneous electron beam-plasma system can be written as

$$f_{e0}(v) = \frac{n_e}{\sqrt{2\pi}v_{\rm th}} e^{-\frac{1}{2}\frac{v^2}{v_{\rm th}^2}} + \frac{n_{eb}}{\sqrt{2\pi}v_{\rm thb}} e^{-\frac{1}{2}\frac{(v-v_d)^2}{v_{\rm thb}^2}} \tag{21}$$

with $v_{\rm th}$ being the electron thermal velocity, v_d the beam velocity and $v_{\rm thb}$ the beam thermal spread. In the simulations presented in this paper, we fix $v_{\rm thb} = v_{\rm th}$ and $v_d = 5v_{\rm th}$. We vary, instead, the shape of the bump corresponding to the term proportional to n_{eb} in Eq. 21, by varying the ratio n_{eb}/n_e. Figure 19 shows $f_{e0}(v)$ for the case $n_{eb}/(n_e + n_{eb}) = 0.004$. The bump is also shown, in the same Figure, in an expanded scale: it gives rise to a positive gradient in a certain velocity range lower than the beam velocity v_d. The electron

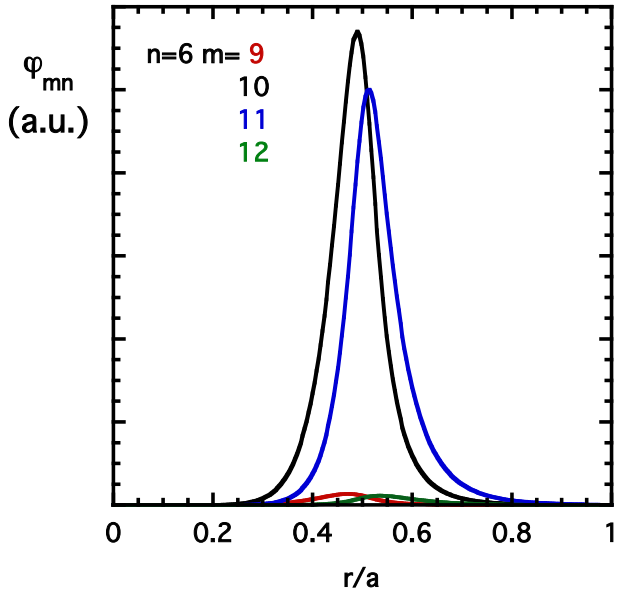

FIG. 12: Radial mode structure of the $n = 6$ TAE as calculated by LIGKA with poloidal harmonics $m = 9 - 12$, with $m = 10, 11$ being the dominant ones.

distribution function is then perturbed by a space dependent amount

$$\delta f_e(x, v) = \nu \cos(kx) f_{e0}(v) \tag{22}$$

with $\nu \ll 1$. In all the cases considered in the following, $k = 0.24/\lambda_{De}$, with $\lambda_{De} \equiv v_{\rm th}/\omega_{pe}$ being the Debye length, and $\omega_{pe} \equiv \sqrt{4\pi n_e e^2/m_e}$ the electron plasma frequency. The perturbed system is periodic in the x direction. In our simulations, a single wavelength $[0, L = 2\pi/k]$ is considered, with particles leaving the system at $x = 0$ or $x = L$ being re-injected, from the opposite side, with the same velocity v.

In this 1D system, the free-energy source for instability is yielded by the positive derivative of $f_{e0}(v)$ associated to the bump, while the transit resonance assumes a very simple form:

$$\omega_{\rm res}(v) = kv. \tag{23}$$

In the case considered in Fig. 19, we find that an unstable mode exists, with frequency

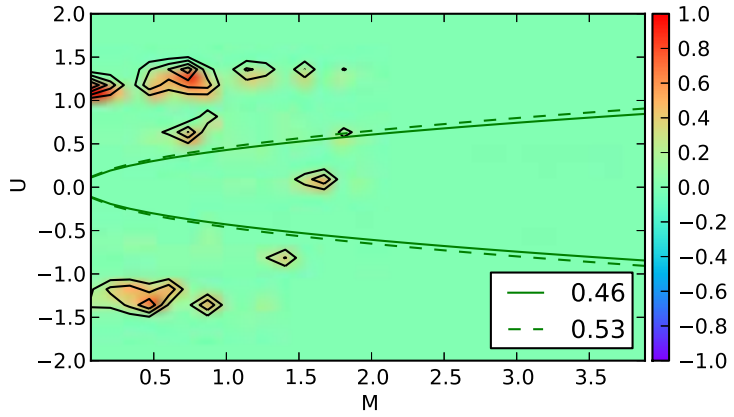

FIG. 13: Power transfer density $P(r, M, U)$, integrated over a toroidal shell centred around the mode peak, for the same case considered in Fig. 12. As in Fig. 3, M and U are reported in units of T_H/Ω_{H0} and $\sqrt{T_H/m_H}$. Passing-trapped particle boundaries evaluated at the inner ($s = 0.46$, solid line) and outer ($s = 0.53$, dashed line) limits of the mode's radial domain are shown.

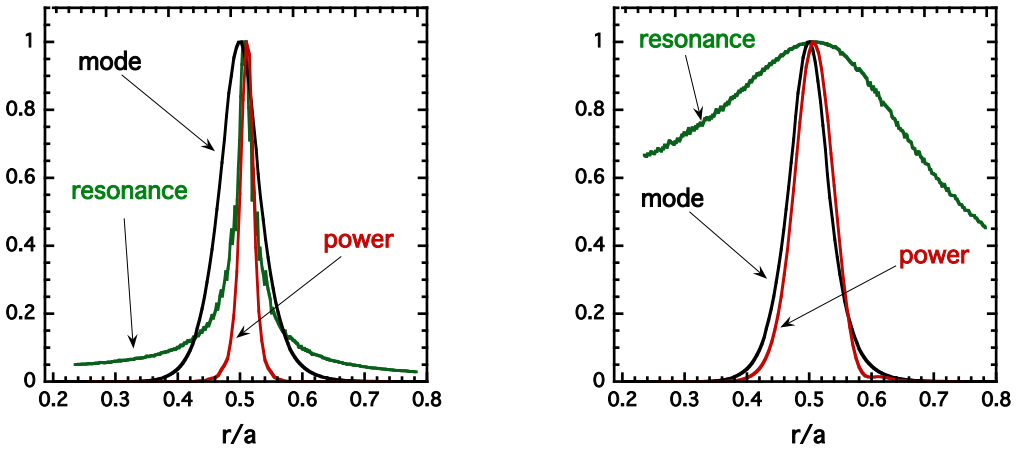

FIG. 14: Same as Fig. 7 for HAGIS TAE simulations. Two different values of the growth rate are considered. The radial extension of power transfer density is limited by resonance width, for low γ values (left); by mode radial width, for large γ values (right).

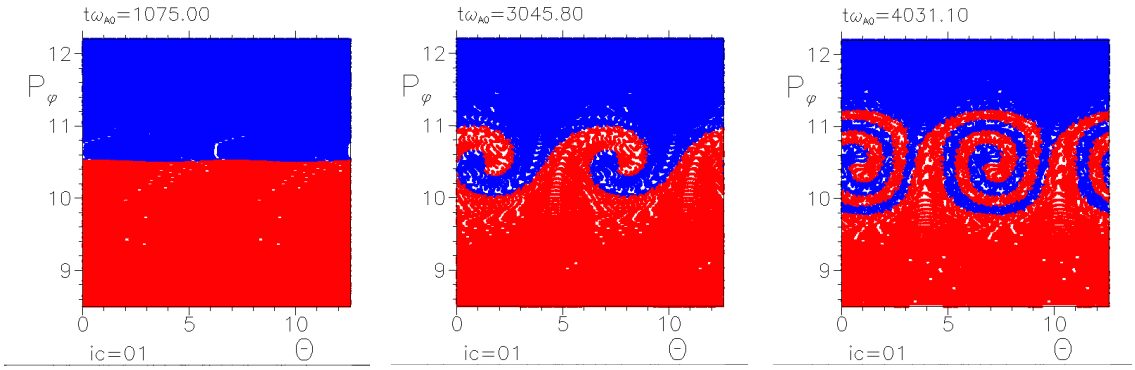

FIG. 15: Same as Fig. 1 for the simulation considered in Fig. 14. Colour convention is the same adopted in Fig. 1. The formation of closed-orbit structures, separated from transit orbits, can be seen in the nonlinear phase (centre and right frames).

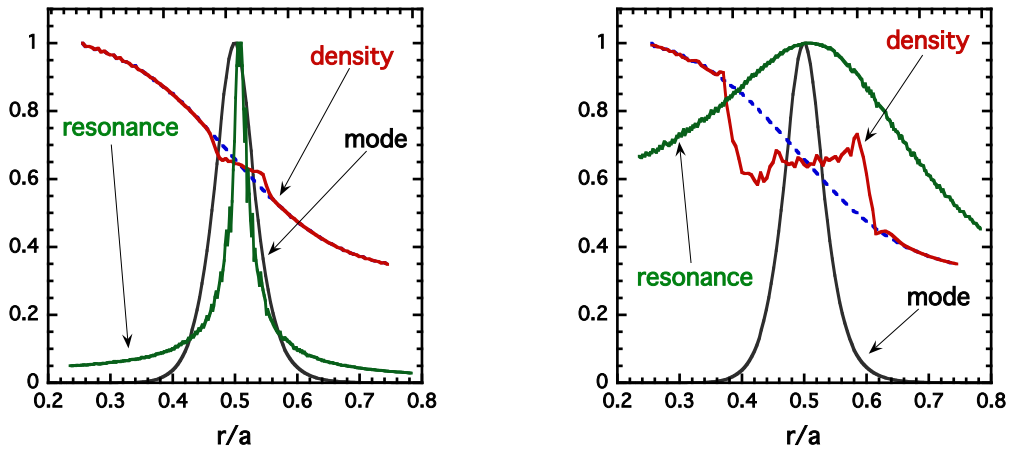

FIG. 16: Same as Fig. 8 for the simulation considered in Fig. 14. The width of the density flattening region at saturation is limited mainly by the finite resonance width, in the lower growth-rate case (left); by the finite mode width, in the larger growth-rate case (right).

$\omega \simeq 1.0732\,\omega_{pe}$ and growth rate $\gamma \simeq 0.013\,\omega_{pe}$. The resonance velocity is then

$$v_{\rm res} = \frac{\omega}{k} \simeq 4.47 v_{\rm th}. \tag{24}$$

Analogously to what we have done for XHMGC and HAGIS simulations, we can analise the behaviour of resonant particles by mapping their orbits on the plane (Θ, v), with the

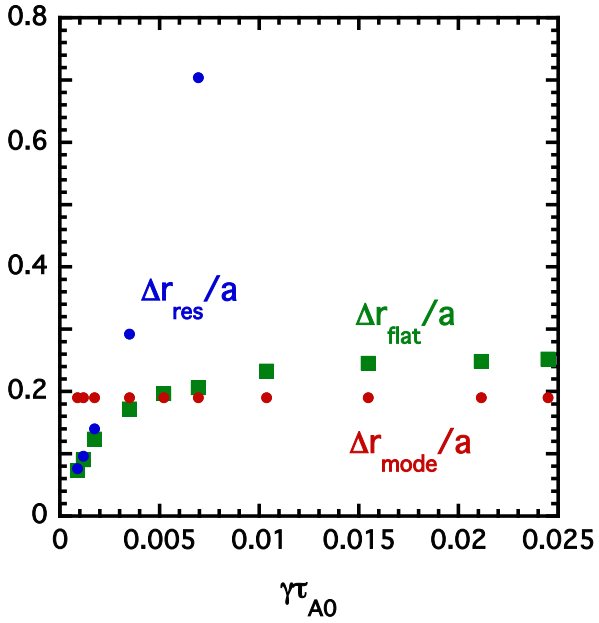

FIG. 17: Radial width of the density flattening region (green squares) at saturation versus γ for HAGIS simulations, compared with mode width (red dots) and resonance width (blue dots). The latter quantities are defined as in Fig. 9.

wave phase given, in this case, by $\Theta = \omega t - kx$. As we are treating a 1D problem, we do not need to cut the phase space into slices, then focusing our investigation on the slice where the power transfer is peaked: indeed, the whole phase space is reduced to a 2D surface. Rather then resorting to the evolution of a suited set of test particles belonging to a particular phase-space slice, we can just analyse the behaviour of a sample of the particles effectively evolved in the simulation. Figure 20 refers to the nonlinear phase of the mode evolution, for the PIC1DP simulation corresponding to the case considered in Fig. 19. The colour convention is analogous to that adopted in Figs. 15 and 1: in this case, blue refers to particles whose initial velocity was lower than $v_{\rm res}$; green, to particles initialised with $v > v_{\rm res}$. As in the XHMGC and HAGIS cases, the formation of closed-orbit structures, separated from transit orbits is shown. It corresponds, here, to a flattening of the velocity-space distribution function around $v_{\rm res}$ and the consequent depression of the $v-$gradient acting as free-energy source for the mode growth. This is shown in Fig. 21, where the resonance structure is reported too.

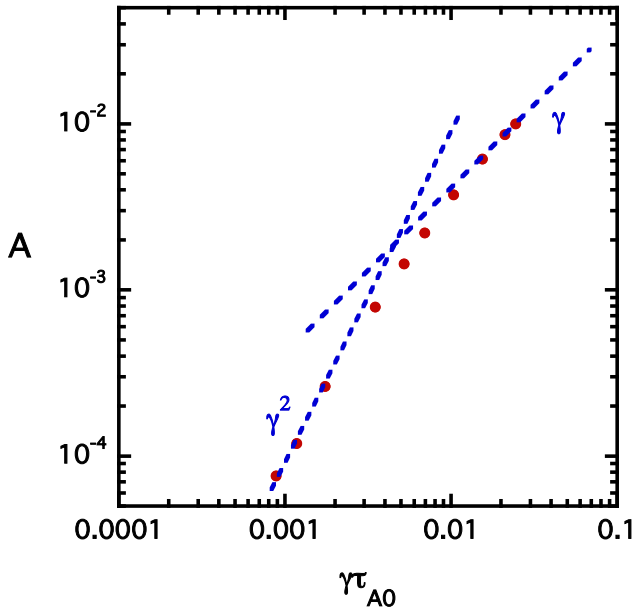

FIG. 18: Scaling of saturation amplitude of scalar potential versus γ for HAGIS simulations. The amplitude is defined as the radial peak of $[\int d\theta d\phi |\varphi(r,\theta,\phi)|^2]^{1/2}$ and is reported in units of T_H/e_H. The reference quadratic and linear γ scaling are also shown.

We see that the width of the flattening region is of the order of the resonance width in the velocity space. In this 1D case, the only constraint on the mode-particle power exchange comes from the finite resonance width, as the mode does not exhibit any structure in the velocity space (more precisely, in the large growth rate limit, characterised by large resonance width, a more stringent constraint could come from the limited width of the velocity region in which the initial distribution gradient is positive). Figure 22 shows how the width of the flattening region at saturation and the resonance width vary with increasing values of γ, corresponding to increasing values of $n_{eb}/(n_e + n_{eb})$. We see that the former is essentially limited by the latter over the whole γ range. For the same cases, Fig. 23 shows that the mode saturation amplitude (here, represented by the perturbed electron density amplitude) scales quadratically with γ, consistently with the results obtained, for XHMGC and HAGIS simulations, in the respective *resonance detuning* regimes.

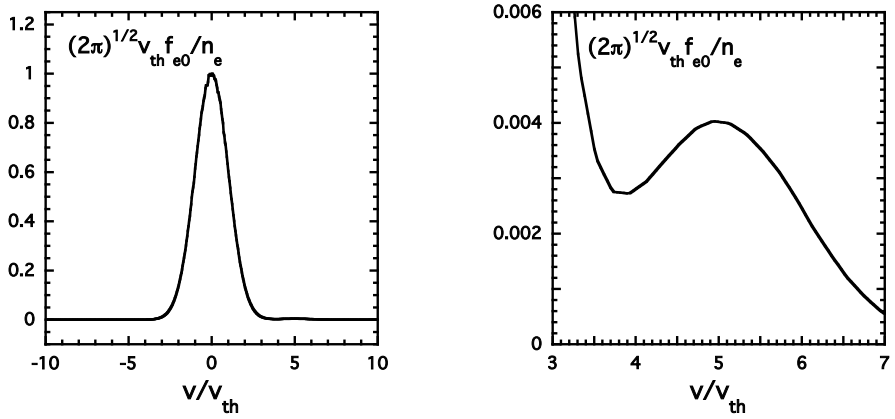

FIG. 19: Normalised initial velocity-space distribution function for PIC1DP simulations (left). The bump corresponding to the term proportional to n_{eb} in Eq. 21 is shown, in the right frame, in an expanded scale. Here, $n_{eb}/(n_e + n_{eb}) = 0.004$.

IV. NONLINEAR PENDULUM MODEL

In Sect III, we have seen that the basic saturation mechanism is the distortion of the resonant-particle distribution function around the resonance (Figs. 8, 16 and 21) , associated to the formation of closed-orbit structures in the (Θ, P_ϕ) (Figs. 1 and 15, for XHMGC and HAGIS) or (Θ, v) plane (Fig. 20, for PIC1DP), which we conventionally indicate as distribution-function *flattening*. In order to get a quantitative analysis of this process, we resort to a simplified model, based on the following nonlinear pendulum system:

$$\frac{dx}{dt} \equiv -A\frac{S}{|S|}\sin\Theta \tag{25}$$

$$\frac{d\Theta}{dt} \equiv Sx \tag{26}$$

$$\frac{dA}{dt} = \bar{\gamma}A \tag{27}$$

$$\bar{\gamma} = \gamma\left\{1 - \frac{\Delta r_{\rm flat}}{\Delta r_{\rm min}}.\right\}. \tag{28}$$

Here, $x \equiv r - r_{\rm res}$ is the radial distance from the resonance surface (where $d\Theta/dt = 0$), $A > 0$ is proportional to the mode amplitude (responsible for the radial drift, Eq.25), and S is related to the radial slope of the resonance frequency: $\omega_{\rm res} \simeq \omega - S(r - r_{\rm res})$, which is responsible for the wave-particle phase change in Eq. 26. The mode amplitude evolution

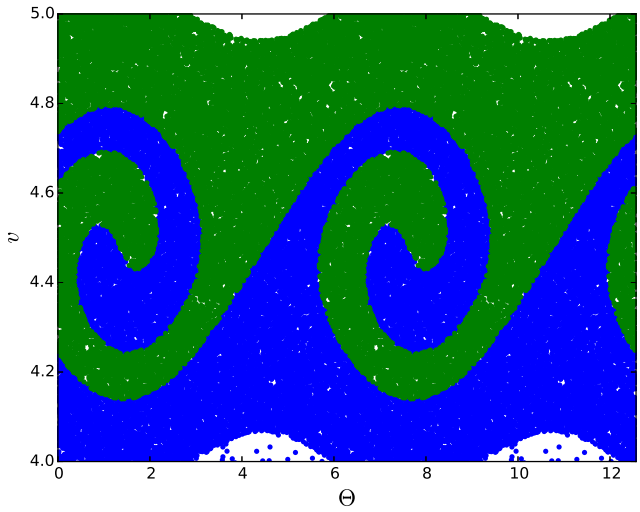

FIG. 20: Particle markers in the (Θ, v) plane in the nonlinear phase of the mode evolution, for a PIC1DP simulation corresponding to the case considered in Fig. 19. Here, $\Theta = \omega t - kx$, and v is normalised to $v_{\rm th}$. Colour convention is analogous to that adopted in Fig. 15: in this case, blue indicates particles whose initial velocity was lower than the resonance value $v_{\rm res} \simeq 4.47 v_{\rm th}$; green, those with initial velocity higher than $v_{\rm res}$. The formation of closed-orbit structures, separated from transit orbits is observed.

is determined by Eq. 27. The effective growth rate $\bar{\gamma}$ is determined, at each time, by the linear growth rate γ and the stabilising effect of the density flattening (here represented by the quantity $\Delta r_{\rm flat}$, to be determined), which progressively erodes the mode-particle power-transfer region, limited by $\Delta r_{\rm min} \equiv \min[\Delta r_{\rm mode}, \Delta r_{\rm res}]$, that is the narrowest of the two widths: the mode width $\Delta r_{\rm mode}$ and the resonance width $\Delta r_{\rm res}$ (cf. Fig. 9).

In the limit of very small linear growth rate, we could evaluate $\Delta r_{\rm flat}$ treating the mode amplitude as a slowly varying quantity. In this "static" limit, the density flattening process would involve the radial width of the separatrix between closed and drifting orbits. We can compute such width noting that, neglecting the time dependence of A, the quantity

$$E(x, \Theta) \equiv \frac{1}{2}\left(\frac{d\Theta}{dt}\right)^2 - A|S|\cos\Theta = \frac{1}{2}(Sx)^2 - A|S|\cos\Theta \tag{29}$$

is a constant of motion. The separatrix crosses the axis $x = 0$ at $\Theta = \pi$. Then, it is

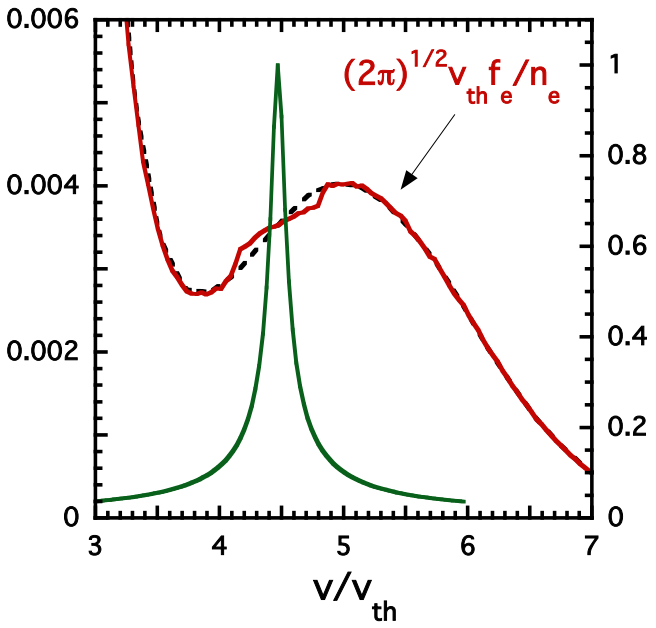

FIG. 21: Velocity-space distribution function at saturation (red solid line), for the same case considered n Fig. 19, compared with the initial distribution function (black dashed line), in the velocity region around $v_{\rm res}$. The profile flattening associated to the formation of closed-orbit structures observed in Fig. 20 is apparent. The resonance structure, represented by the quantity $\gamma/[(\omega-\omega_{\rm res}(v))^2+\gamma^2]^{-1/2}$ is shown for comparison.

characterised by a value of E given by

$$E_{\rm sep} \equiv E(0,\pi) = A|S|. \tag{30}$$

We can then compute its half width $x_{\rm sep}$ from the condition

$$E(x_{\rm sep},0) = E_{\rm sep}, \tag{31}$$

that is

$$\frac{1}{2}(Sx_{\rm sep})^2 - A|S| = A|S|; \tag{32}$$

from which

$$\Delta r_{\rm flat}^{\rm static} \simeq 2\,|x_{\rm sep}| = 4\left(\frac{A}{|S|}\right)^{1/2}. \tag{33}$$

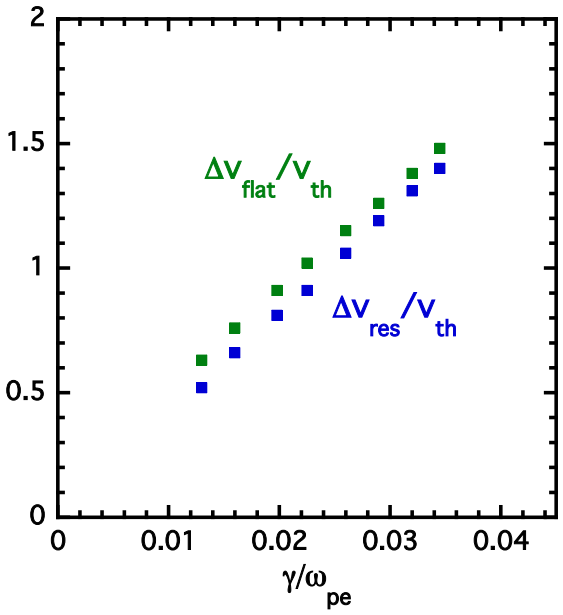

FIG. 22: Width of the flattening region in the velocity space at saturation versus γ compared with the resonance width, for PIC1DP simulations. Increasing values of γ corresponds to increasing values of $n_{eb}/(n_e + n_{eb})$.

We observe that this *static* approach, in which the mode amplitude A is treated as a constant while evaluating its effect on the density flattening, is appropriate only in the very low growth rate limit: $\gamma T_{\rm orb} \ll 1$, with $T_{\rm orb}$ being the time needed for a particle to complete its closed orbit. Even in this limit, however, $T_{\rm orb}$ is an increasing function of $\Theta_0 \in [0, \pi[$, where Θ_0 is the value of Θ at which the orbit crosses the axis $x = 0$:

$$T_{\rm orb}(\Theta_0) = \frac{4}{(|S|A)^{1/2}} K(\sin^2 \frac{\Theta_0}{2}), \tag{34}$$

with K being the elliptic integral of the first kind [53]. Deeply wave-trapped particles ($\Theta_0 \to 0$) will then be characterised by a smaller $T_{\rm orb}$ than particles close to the separatrix ($\Theta_0 \to \pi$); for the latter particles, for which the bounce time tends to infinity, the static-limit assumption fails even for low values of the linear growth rate. It is then worth modifying the estimate of $\Delta r_{\rm flat}$ given in Eq. 33 by assuming that the density flattening involves, at a certain time, only a fraction of the whole region contained within the virtual separatrix

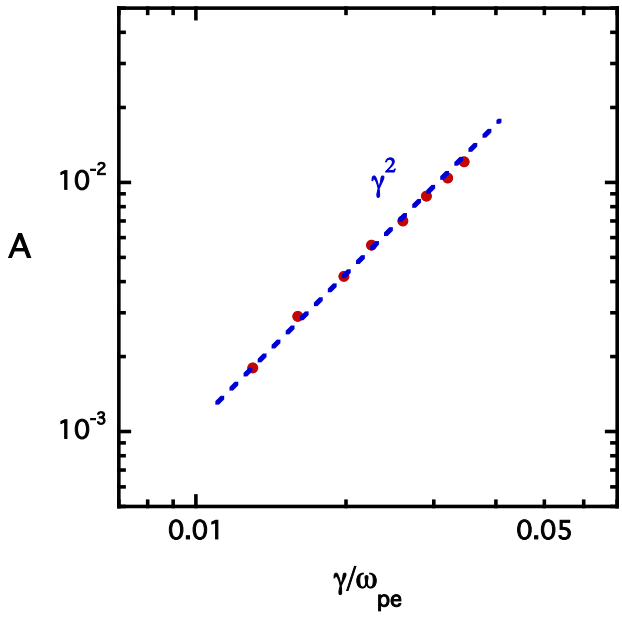

FIG. 23: Scaling of saturation amplitude of the perturbed electron density (normalised to the initial electron density) versus γ for PIC1DP simulations. The reference quadratic γ scaling is also shown.

that would correspond, in the static limit, to the actual instantaneous amplitude. We write this condition in the form

$$\Delta r_{\rm flat} \simeq 2\,|x_{\rm max}|\,, \tag{35}$$

where $|x_{\rm max}|$ is the largest radial excursion observed, at the considered time, among all the particles captured by the wave (that is, particles that have crossed the resonance surface, $x = 0$). Figure 24 shows the plot of traces of particle trajectories in the plane (Θ, x) evolved according to Eqs. 25-28 and 35. The density flattening width, Eq. 35, and the width that the separatrix between closed and open trajectories would have for a mode amplitude statically equal to that dynamically reached at the considered time are evidenced. It is apparent that the latter width (corresponding to the static-limit evaluation of the flattening region, Eq. 33) is much larger than the former. This is confirmed by Fig. 25, comparing the time evolution of $\Delta r_{\rm flat}$ and $\Delta r_{\rm flat}^{\rm static}$

The above model, with $\Delta r_{\rm flat}$ defined by Eq. 35, appears to be suited to mimic simulation results presented in Sect. III with respect to the saturation dynamics. Figure 26 shows indeed

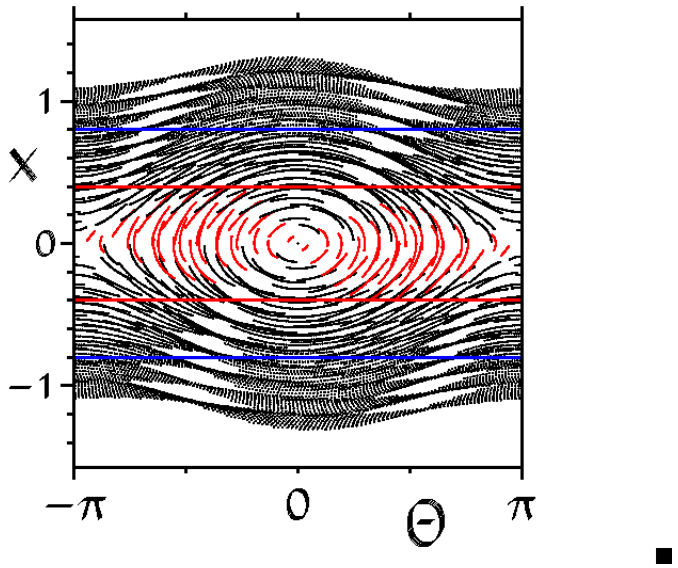

FIG. 24: Traces of particle trajectories in the plane (Θ, x) evolved according to the nonlinear pendulum model (Eqs. 25-28), for $S = 0.02$, $\Delta r_{\rm mode} = 0.8$ and $\gamma = 0.016$. Red traces correspond to particles that have already crossed, at the considered time, the resonance ($x = 0$). Solid horizontal red lines indicate the limits of the region explored by such particles; their distance plays the role, in the model, of the density flattening width $\Delta r_{\rm flat}$. Blue lines delimit the width $\Delta r_{\rm flat}^{\rm static}$ that the separatrix between closed and open trajectories would have for a mode amplitude statically equal to that dynamically reached at the considered time. Note that the plot refers to the saturation time, corresponding to $\Delta r_{\rm flat} = \Delta r_{\rm min}$, with $\Delta r_{\rm min} \equiv \Delta r_{\rm mode}$ for the present case.

the scaling of saturation mode amplitude versus γ obtained by numerical solution of Eqs. 25-28 and 35. It can be seen that a transition from quadratic to linear scaling is observed, as γ increases, causing $\Delta r_{\rm res}$ to exceed $\Delta r_{\rm mode}$.

Let us try to get an approximate analytic solution of this system, in order to interpret this behaviour. To this aim, we assume that $\Delta r_{\rm flat}$ is mainly determined, at each time, by particles that satisfy, while evolving from resonance-crossing time to the actual time, the

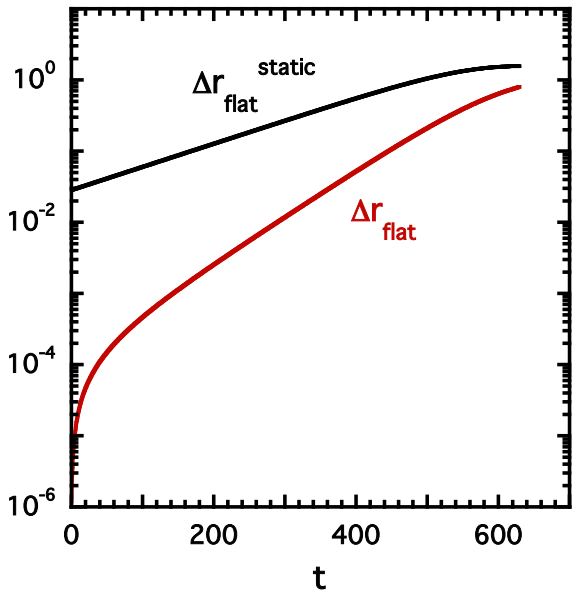

FIG. 25: Flattening width $\Delta r_{\rm flat}$, defined as the maximum x distance among particles that have crossed the resonance (Eq. 35), compared with the naive static-limit solution $\Delta r_{\rm flat}^{\rm static}$ yielded by Eq. 33. It is apparent that the static solution largely overestimate the effective flattening width.

condition $\sin\Theta \simeq 1$. We also assume that the quantity $|x_{\rm max}|$, which determines $\Delta r_{\rm flat}$, can be computed by following the same couple of particles (crossing the resonance in opposite directions) for the entire evolution of the system. This assumption, corresponding to measuring the whole particle population behaviour from that of a couple of *leading* particles, allows us to reduce our system to the following one:

$$\frac{d|x_{\rm max}^{\rm approx}|}{dt} \simeq A \tag{36}$$

$$\frac{dA}{dt} = \bar{\gamma} A \tag{37}$$

$$\bar{\gamma} \simeq \gamma \left\{ 1 - \frac{2|x_{\rm max}^{\rm approx}|}{\Delta r_{\rm min}} \right\}, \tag{38}$$

or

$$\gamma \left\{ 1 - \frac{2|x_{\rm max}^{\rm approx}|}{\Delta r_{\rm min}} \right\} \frac{d|x_{\rm max}^{\rm approx}|}{dt} = \frac{dA}{dt}. \tag{39}$$

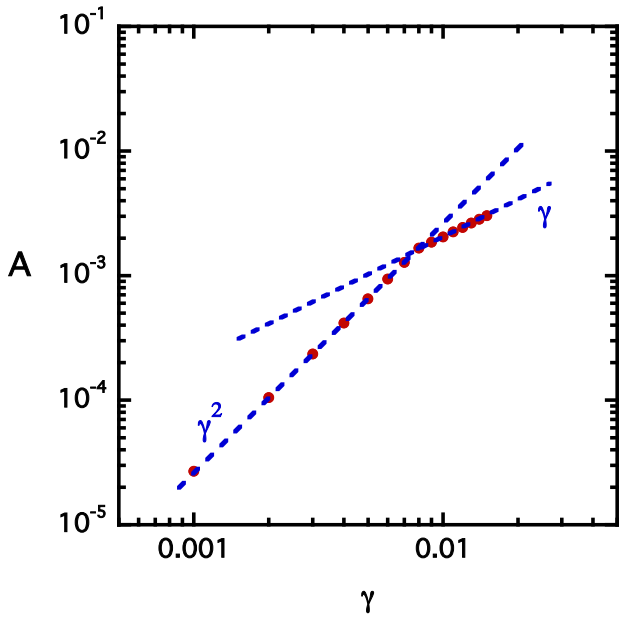

FIG. 26: Scaling of saturation mode amplitude versus γ for simulations of the nonlinear pendulum model. The reference quadratic and linear γ scaling are also shown.

Equation 39 yields the solution

$$\Delta r_{\rm flat}^{\rm approx} \equiv 2|x_{\rm max}^{\rm approx}| = \Delta r_{\rm min}\left[1-\left(1-\frac{4A}{\gamma\Delta r_{\rm min}}\right)^{1/2}\right]. \qquad (40)$$

Figure 27 compare the exact numerical solution for the flattening width, as defined by Eq. 35, with the approximate solution, Eq. 40. The agreement is very satisfactory. From the same Figure, it can be seen that $|\sin(\Theta)| \simeq 1$, essentially constant along the particle motion, is a good approximation, as far as we are interested in the behaviour of the largest-excursion particles.

Figure 28 plots the exact solution, $\Delta r_{\rm flat}$, versus the approximate one, $\Delta r_{\rm flat}^{\rm approx}$, for different cases, characterised by different values of γ. It is apparent that the dependence on the linear growth rate is well retained by the approximate solution, as well.

In order to get simple expression for the scaling of the saturation mode amplitude with

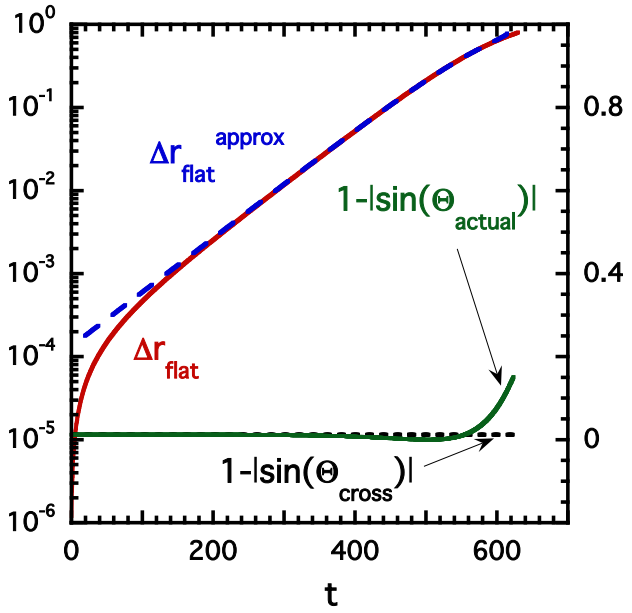

FIG. 27: Flattening width, defined as in Eq. 35, compared with the approximate solution yielded by Eq. 40. Deviations of $|\sin(\Theta_{\rm cross})|$ and $|\sin(\Theta_{\rm actual})|$ from 1 are also reported, versus time, for the particles that, at each time, exhibit the largest x excursion from the resonance. Here, $\Theta_{\rm cross}$ is the phase value at which the particle has crossed the resonance; $\Theta_{\rm actual}$ is the phase value of the same particle at time t. It can be seen that $|\sin(\Theta)| \approx 1$ is a good approximation, as far as we are interested in the behaviour of the largest-excursion particles.

the growth rate, we consider the low-amplitude limit of $\Delta r_{\rm flat}^{\rm approx}$:

$$\Delta r_{\rm flat}^{\rm approx} \simeq \frac{2A}{\gamma}. \tag{41}$$

The exact solution $\Delta r_{\rm flat}$ is plotted versus this low-amplitude limit solution in Fig. 29. We can then obtain an approximate expression for the saturation condition:

$$A^{\rm sat} \simeq \frac{\Delta r_{\rm min}\gamma}{2} \tag{42}$$

We can then evaluate $\Delta r_{\rm res}$, consistently with the linearisation of $\omega_{\rm res}$ around $r_{\rm res}$, as

$$\Delta r_{\rm res} \simeq 2\frac{\gamma}{|S|}. \tag{43}$$

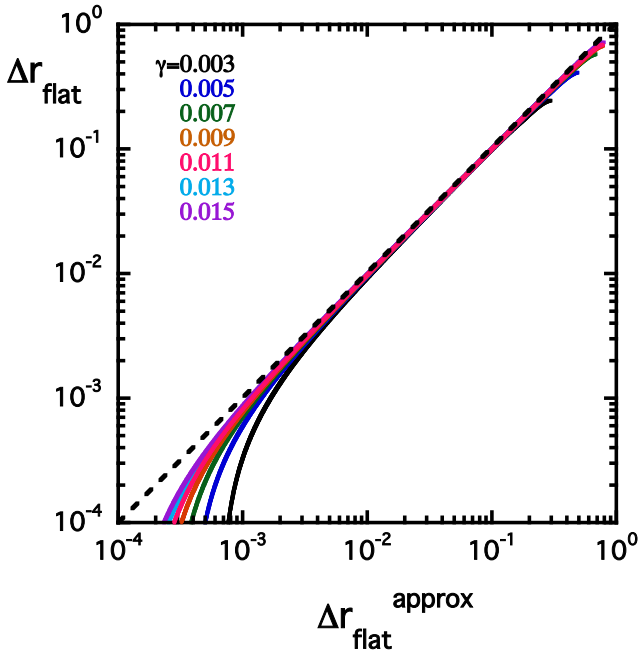

FIG. 28: Flattening width, defined as in Eq. 35, plotted versus the approximate solution yielded by Eq. 40, for different cases, characterised by different values of the linear growth rate (the dashed line would represent the perfect conincidence between the two quantities). The dependence on γ is apparently well retained by the approximate solution.

Let us assume, instead, that the mode width does not depend on the linear growth rate (cf. Fig. 9). For $\Delta r_{\rm res} < \Delta r_{\rm mode}$, we then find

$$A^{\rm sat} \simeq \frac{\Delta r_{\rm res}\gamma}{2} \simeq \frac{\gamma^2}{|S|}. \tag{44}$$

For $\Delta r_{\rm mode} < \Delta r_{\rm res}$, we find

$$A^{\rm sat} \simeq \frac{\Delta r_{\rm mode}\gamma}{2}. \tag{45}$$

These results appear to be consistent with the quadratic and linear scalings observed, for low and high γ, respectively, in Fig. 26.

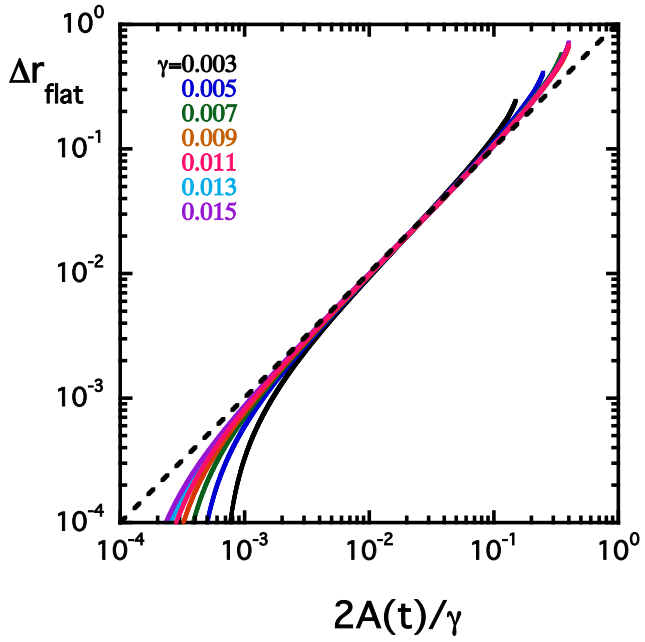

FIG. 29: Flattening width, defined as in Eq. 35, plotted versus the solution yielded by Eq. 41, for the same case considered in Fig. 28. As expected, the agreement is good for not too large amplitudes.

V. APPLICATION OF THE PENDULUM MODEL PREDICTIONS TO DIFFERENT CODE RESULTS

In the present Section we check whether saturation dynamics observed in the simulations presented in Sect. III can be interpreted in terms of the results obtained from the nonlinear pendulum model. In Sect. IV, we have seen that the transition from a quadratic to a linear growth-rate dependence of the mode amplitude at saturation is consistent with the evolution of the radial width of the density flattening region specified by the approximate solutions given by Eq. 40 or, for not too large mode amplitudes, Eq. 41. Noting that in the nonlinear pendulum model the existence of a density profile is only assumed, and its evolution represented by the quantity $\Delta r_{\rm flat}$ conventionally defined by Eq. 35, we have first to check whether an analogous definition applied to our plasma simulations is suited to measure the effective density flattening process. Figure 30 compares the radial separation of the steepest resonant-particle density gradients with the flattening width, defined as in Sect. IV, Eq. 35.

The former quantity can be considered an effective measure of the density flattening; the latter apparently reproduce it in a satisfactory way (in the following, we shall indicate it as density-flattening width). The maximum radial spread among particles that have completed a full bounce in the (Θ, P_ϕ) plane is also reported for comparison. This quantity does not represent a good approximation of the gradients separation, consistently with the fact that particle motion determining density flattening can experience only a limited amount of the phase variation due to the shift from the resonance radius. The formation of closed orbits (full bounce) requires a longer time. Figures 31 and 32 shows analogous quantities for HAGIS and PIC1DP simulations.

We can now check the validity of the approximate pendulum-model prediction, Eq. 41, for the evolution of the density-flattening width. Figure 33 plots the density-flattening width, defined as in Fig. 25, versus the corresponding approximate prediction, for several XHMGC code simulations, characterised by different linear growth rates. Figures 34 and 35 report the corresponding results for HAGIS and, respectively, PIC1DP simulations (in the latter case, relative to the flattening of the velocity-space distribution function). It is apparent that the proportionality of the flattening width to the ratio between the instantaneous mode amplitude and the linear growth rate is well satisfied in all cases. We can then conclude that the analysis carried on in Sect. IV yields a satisfactory approximation of the nonlinear evolution both of bump-on-tail instability and more complex single toroidal number Alfvén gap modes.

VI. EXPECTED RADIAL DISPLACEMENT OF FAST IONS

In the present Section, we will estimate, from the simulation results presented in the previous sections, an upper limit to the expected radial displacement of fast ions induced by single toroidal number gap modes. We will consider only passing fast ions in the presence of BAEs, TAEs or EAEs. The most unstable gap modes in next-generation burning plasmas, like those corresponding to ITER scenarios, are expected to be characterised by n of the order of some tens[5]. For such large-n modes, the radial width of the single poloidal harmonic can be estimated as

$$\Delta r_m^{\mathrm{harm}} \simeq \frac{r_m^{\mathrm{gap}}}{m} \simeq \frac{r_m^{\mathrm{gap}}}{nq} \tag{46}$$

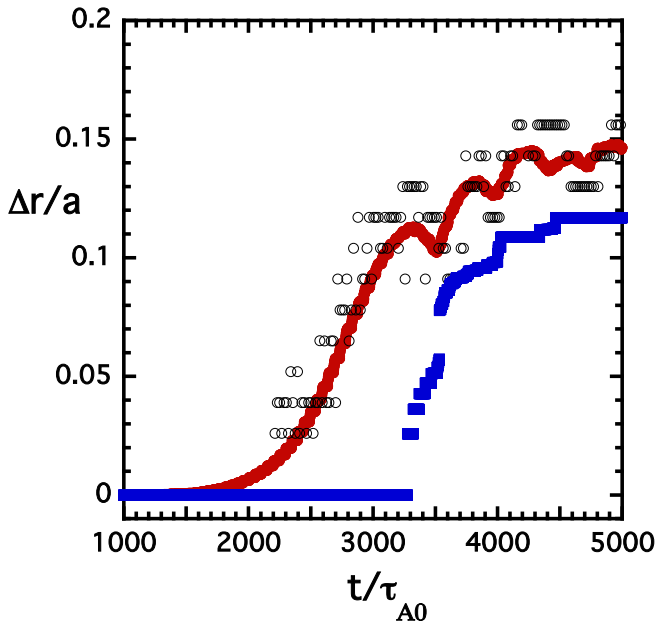

FIG. 30: XHMGC results: radial separation of the steepest density gradients (black circles) versus time, compared with the flattening width (red dots), defined as in Sect. IV, Eq. 35. Note that the values corresponding to the former quantity exhibit both noisy and stepwise behaviour; this is due to the fact that, for a given number of test particles, they result from the compromise between two conflicting requirements: reducing the numerical noise (by adopting a coarser radial grid for computing the density profile), and increasing the spatial resolution (by adopting a finer grid). The maximum radial spread among particles that have completed a full bounce in the (Θ, P_ϕ) plane is also reported for comparison (blue squares).

with $r_m^{\rm gap}$ being the radial localisation of the gap implicitly yielded by

$$q(r_m^{\rm gap}) = \frac{m+\alpha}{n}, \tag{47}$$

with $\alpha = 0$, $1/2$ or 1, for, respectively, BAEs, TAEs and EAEs. Here and in the following, for simplicity, we treat the magnetic equilibrium in the large-aspect-ratio circular-magnetic-surface limit. From Eq. 47, we can compute the radial distance between the considered gap

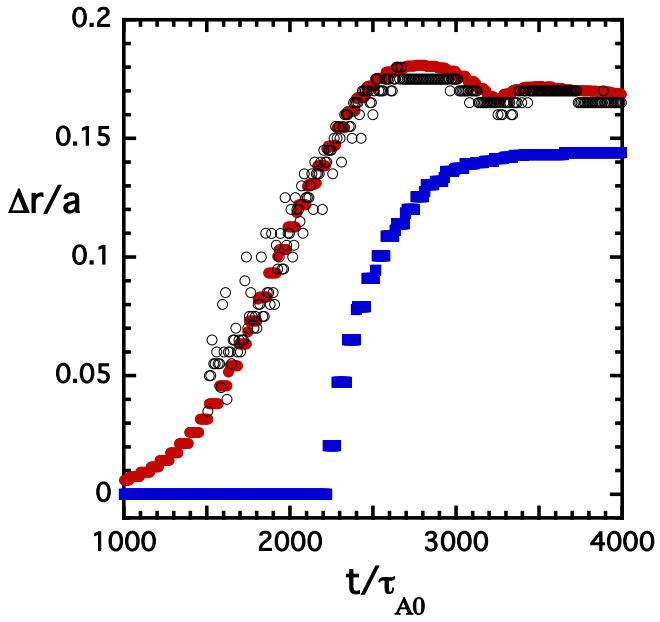

FIG. 31: Same as Fig. 30 for a HAGIS simulation.

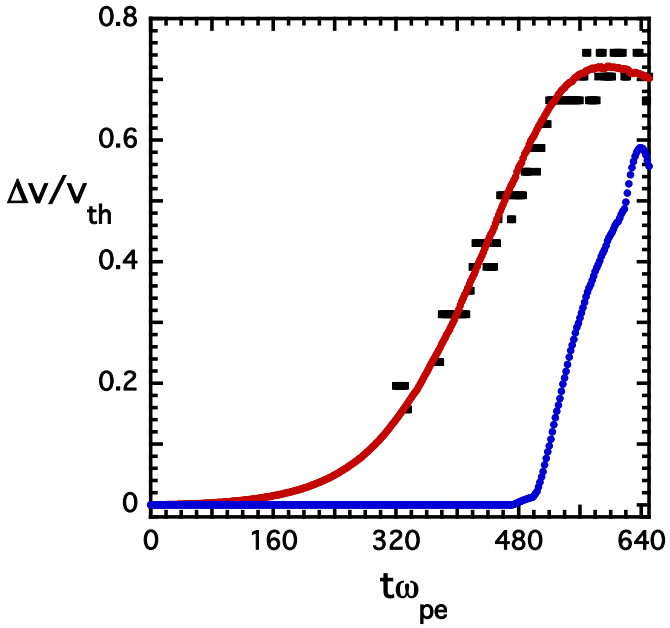

FIG. 32: Same as Fig. 30 for a PIC1DP simulation.

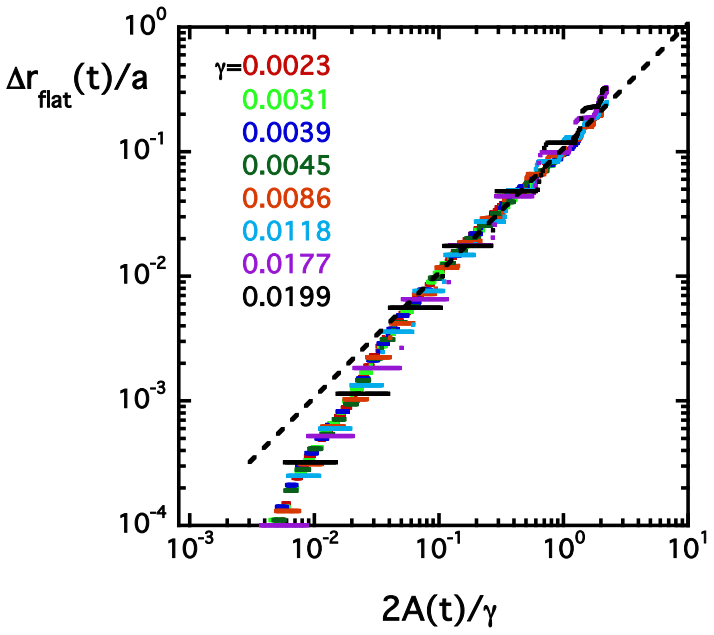

FIG. 33: Flattening width, defined as in Fig. 25, versus the approximate solution yielded by Eq. 41 for several XHMGC simulations, characterised by different linear growth rates. The dashed line represents the pure proportionality relationship between the two quantities. Here, the growth rates is reported in units of $1/\tau_{A0}$; the amplitude of the scalar potential, in units of T_H/e_H.

and those relative to adjacent poloidal harmonics as

$$\Delta r_m^{\rm gap} \simeq \frac{r_m^{\rm gap}}{nq(r_m^{\rm gap})|s|}, \tag{48}$$

with s being the magnetic shear, defined as

$$s \equiv \left(r\frac{q'}{q}\right)_{r=r_m^{\rm gap}}. \tag{49}$$

We can then distinguish two regimes with respect to the mode structure: a low-shear regime ($s << 1$), in which the mode structure is constituted essentially by a single poloidal harmonic (for BAEs) or by a couple of harmonics (m and $m+1$, for TAEs; m and $m+2$ for EAEs), and a high-shear regime ($s \gtrsim 1$) in which the radial distance between different-harmonic gaps is smaller than the width of the single harmonic (cf. Eqs. 46 and 48), and a global mode exists, formed by many harmonics.

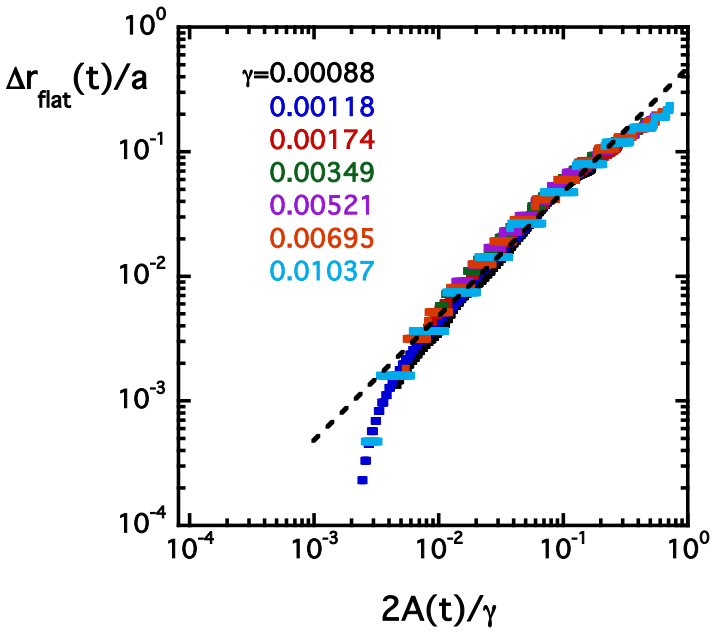

FIG. 34: Same as Fig. 33, for several HAGIS simulations, characterised by different linear growth rates. Here, the growth rates is reported in units of $1/\tau_{A0}$; the amplitude of the scalar potential, in units of T_H/e_H.

In the previous Sections, we have seen that the radial displacement of resonant fast ions gives rise to a density flattening over a radial region whose width is approximately given, at saturation, by

$$\Delta r_{\rm flat}^{\rm sat} \simeq \min\left[\Delta r_{\rm res}, \Delta r_{\rm mode}\right], \tag{50}$$

Let us estimate, in the two shear regimes just identified, the quantities $\Delta r_{\rm res}$ and $\Delta r_{\rm mode}$.

In the low-shear regime, $\Delta r_{\rm mode}$ corresponds to the width of the single harmonic:

$$\Delta r_{\rm mode} \simeq \frac{r_m^{\rm gap}}{nq(r_m^{\rm gap})}. \tag{51}$$

The quantity $\Delta r_{\rm res}$ can be evaluated, in terms of the resonance frequency (for passing fast ions),

$$\omega_{\rm res}(r,m,k) \simeq [(nq-m)\sigma + k]\omega_b, \tag{52}$$

as

$$\Delta r_{\rm res} \simeq \gamma \left|\frac{\partial \omega_{\rm res}}{\partial r}\right|^{-1}_{r=r_m^{\rm gap}}. \tag{53}$$

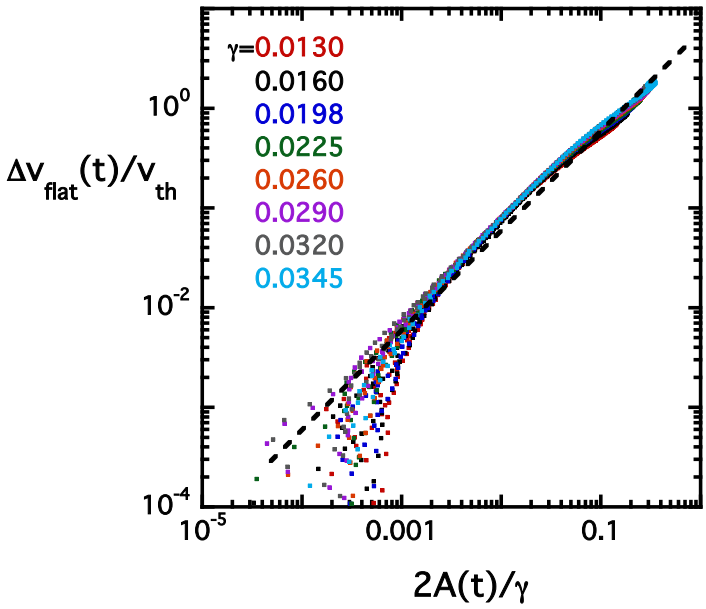

FIG. 35: Same as Fig. 33, for several PIC1DP simulations, characterised by different linear growth rates. Note that in this case, the flattening is measured in the velocity space. Here, the growth rate is reported in units of ω_{pe}; the amplitude of the perturbed electron density is normalised to the initial electron density.

This conventional definition correspond to the half width of the resonance structure defined in Fig. 7 at $1/\sqrt{2}$ of its maximum. From $\omega_b \simeq \sigma U/(qR_0)$, we get

$$\frac{\partial \omega_{\rm res}}{\partial r} \simeq \frac{U'}{U}\omega_{\rm res} + \frac{(m-k\sigma)}{q}\frac{U}{R_0}\frac{q'}{q}. \tag{54}$$

with $U = U(r)$ determined, once fixed $C = C_0$ and $M = M_0$, by the following equation:

$$U^2 - \frac{2\omega R_0}{n}U + \frac{2C_0}{nm_H} + \frac{2M_0\Omega_H}{m_H} - \frac{2\omega e_H R_0}{nm_H c}(\psi_{\rm eq} - \psi_{\rm eq0}) = 0. \tag{55}$$

We then get

$$U'\left[U - \frac{\omega R_0}{n}\right] \simeq \frac{\omega e_H R_0}{nm_H c}\frac{d\psi_{\rm eq}}{dr} \tag{56}$$

or

$$\frac{U'}{U} \simeq \frac{\omega\Omega_H r}{(\omega R_0 - nU)qU}. \tag{57}$$

From Eqs. 47 and 52 and the resonance condition

$$\omega_{\rm res}(r_m^{\rm gap}) = \omega, \tag{58}$$

we obtain

$$U(r_m^{\rm gap}) \simeq \sigma \frac{qR_0\omega}{|\alpha + k\sigma|} \tag{59}$$

and, in the limit of large n,

$$\left|\frac{\partial \omega_{\rm res}}{\partial r}\right|_{r_m^{\rm gap}} \simeq \left|\frac{nsq\omega\sigma}{|\alpha + k\sigma| r} - \frac{(\alpha + k\sigma)^2}{nq^3R_0^2}\frac{r}{\rho_H}v_H\right|_{r_m^{\rm gap}}. \tag{60}$$

Note that for BAEs ($\alpha = 0$) only bounce harmonics $k \neq 0$ can be taken into account.

We expect that most unstable modes are those characterised by orbit widths of the order of the width of the dominant poloidal harmonic:

$$\Delta r_{\rm orbit} \simeq \frac{qv_A}{\Omega_H} \approx \Delta r_m^{\rm harm}; \tag{61}$$

that is

$$\frac{r_m^{\rm gap}}{\rho_H} \simeq nq^2\frac{v_A}{v_H}. \tag{62}$$

For such modes, Eqs. 53 and 60 yield

$$\Delta r_{\rm res} \simeq \frac{\gamma}{\omega}\frac{r_m^{\rm gap}}{nq(r_m^{\rm gap})}K. \tag{63}$$

withe

$$K \equiv \left|\frac{s\sigma}{|\alpha + k\sigma|} - \frac{(\alpha + k\sigma)^2 v_A r}{nq^2R_0^2\omega}\right|^{-1}_{r_m^{\rm gap}}. \tag{64}$$

We see that, notwithstanding the ratio γ/ω is expected to be quite small in burning-plasma scenarios, mode saturation can enter the radial decoupling regime ($\Delta r_{\rm res} > \Delta r_{\rm mode}$) if the factor K is large enough. Even in such cases, however, the width of density-flattening region is limited by the width of the single poloidal harmonic.

In the high-shear regime ($|s| \gtrsim 1$), the question is whether the width of the density-flattening region at saturation can be limited by the potentially large width of the envelope of the many harmonics constituting the global mode. If this were the case, even the effect of a single toroidal number gap mode could be deleterious for fast-ion confinement. In favour of a positive answer, a global (multi-harmonic) resonance mechanism could be envisaged, making the effective resonance width large enough. This mechanism should work as follows. A particle, resonating, at the gap position $r_m^{\rm gap}$, with the harmonic (or the harmonics)

yielding that gap is displaced by a radial amount of the same order of the gap separation $\Delta r_m^{\rm gap}$, until it mainly feels the interaction with the adjacent harmonic (or harmonics). If the resonance frequency at the new position (with the new couple of harmonics) is still adequately satisfied, the particle can be further displaced up to the next gap, and so on. Differently form the previous calculation of $\Delta r_{\rm res}$, in which we derived $\omega_{\rm res}$ with respect to r, while keeping m and k constant, in the present case we have to keep k constant, while varying m and $r_m^{\rm gap}$ at the same time, by discrete amounts:

$$\Delta r_{\rm res}^{\rm global} \simeq \gamma \left| \frac{\Delta \omega_{\rm res}}{\Delta r} \right|^{-1}_{r=r_m^{\rm gap}}, \tag{65}$$

with

$$\frac{\Delta \omega_{\rm res}}{\Delta r}(r_m^{\rm gap}) \equiv \frac{\omega_{\rm res}(r_{m+\Delta m}^{\rm gap}, m+\Delta m, k) - \omega_{\rm res}(r_m^{\rm gap}, m, k)}{r_{m+\Delta m}^{\rm gap} - r_m^{\rm gap}}. \tag{66}$$

Figure 36 shows, for a generic case, the frequency values entering the discrete derivative, Eq. 66. Expanding $U(r_{m+\Delta m}^{\rm gap})$ around $r_m^{\rm gap}$ as

$$U(r_{m+\Delta m}^{\rm gap}) \simeq U(r_m^{\rm gap}) + U'(r_m^{\rm gap})(r_{m+\Delta m}^{\rm gap} - r_m^{\rm gap}) \tag{67}$$

and using the relationships

$$q(r_{m+\Delta m}^{\rm gap}) = q(r_m^{\rm gap}) + \frac{\Delta m}{n} \tag{68}$$

and

$$r_{m+\Delta m}^{\rm gap} - r_m^{\rm gap} \simeq \frac{\Delta m}{n} \frac{r_m^{\rm gap}}{q(r_m^{\rm gap}) s}, \tag{69}$$

we find

$$\Delta r_{\rm res}^{\rm global} \simeq \frac{\gamma}{\omega} \left| \frac{s}{r} + \frac{v_A(\alpha + k\sigma)^2}{R_0^2 \omega q} \right|^{-1}_{r=r_m^{\rm gap}} \tag{70}$$

For TAEs and EAEs, we can approximate ω by the expression

$$\omega \simeq \alpha \frac{v_A}{q R_0}. \tag{71}$$

We then get

$$(\Delta r_{\rm res}^{\rm global})_{\rm TAE,EAE} \simeq \frac{\gamma}{\omega} \frac{r_m^{\rm gap}}{|s|} \simeq \frac{\gamma}{\omega} \frac{nq(r_m^{\rm gap})}{|s|} \Delta r_m^{\rm harm}. \tag{72}$$

As $nq >> 1$, if such global resonance mechanism were effective, the density flattening could extend for a radial region larger than the single poloidal harmonic, in spite of not too large growth rates. In order the global resonance can act, however, the resonant particle needs to be displaced by the original dominant harmonic by a radial distance of the order

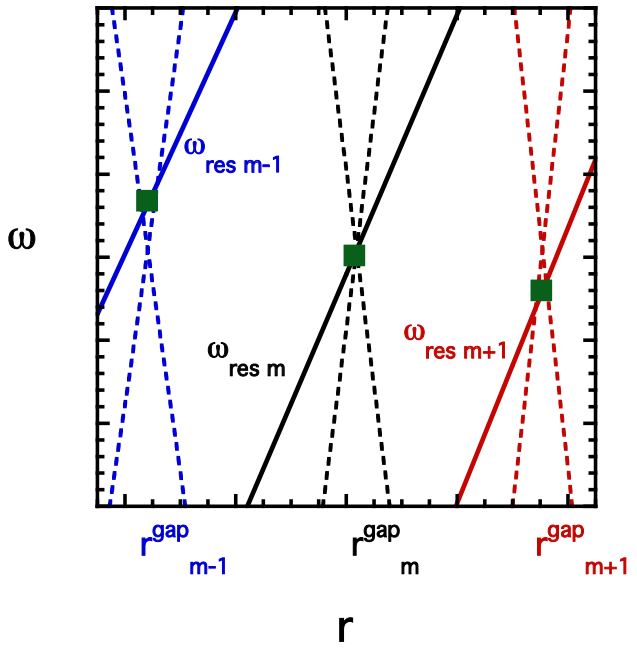

FIG. 36: Radial profile $\omega_{\rm res}(r, m', k)$ of the resonance frequency, for three poloidal harmonics $m' = m-1, m, m+1$ and the same value of k (solid lines). The localisation $r^{\rm gap}_{m'}$ of the corresponding adjacent gaps is evidenced (for simplicity, only the cylindric-limit continua are represented, by dashed lines, for the relevant harmonics). Green squares show the frequency values, $\omega_{\rm res}(r^{\rm gap}_{m'}, m', k)$, entering the discrete derivative, Eq. 66.

of $\Delta r^{\rm gap}_m$. From Eq. 63, however, we see that in the high-shear regime the expression for the single-harmonic resonance width $\Delta r_{\rm res}$ can be approximated as

$$(\Delta r_{\rm res})_{\rm TAE,EAE} \simeq \frac{\gamma}{\omega} \left|\alpha + k\sigma\right| \Delta r^{\rm gap}_m << \Delta r^{\rm gap}_m. \tag{73}$$

We then see that the condition $|s| \gtrsim 1$, required for a global mode to exist, makes the radial profile of the single-harmonic resonance frequency so sharp that the radial displacement of the resonant particles, for low/moderate growth rates, is limited to a small fraction of the distance between adjacent gaps (and, *a fortiori*, the radial width of the single harmonic).

For BAEs, the real frequency is approximately given by

$$\omega \simeq \left(\frac{7}{2}\frac{T_i}{m_i} + \frac{2T_e}{m_i}\right)^{1/2} \frac{1}{R_0} \equiv \left(\frac{7}{2} + \frac{2T_e}{T_i}\right)^{1/2} \beta_i^{1/2} \frac{v_A}{R_0}, \tag{74}$$

with T_e and T_i being, respectively, the bulk-electron and bulk-ion temperatures, and β_i the ratio between bulk-ion kinetic and magnetic pressure. Equations 72 and 73 are replaced by

$$(\Delta r_{\rm res}^{\rm global})_{\rm BAE} \simeq \frac{\gamma}{\omega}\left|\frac{s}{r}+\frac{k^2}{\beta_i^{1/2}qR_0\left(\frac{7}{2}+\frac{2T_e}{T_i}\right)^{1/2}}\right|^{-1}_{r=r_m^{\rm gap}} \tag{75}$$

and

$$(\Delta r_{\rm res})_{\rm BAE} \simeq \frac{\gamma}{\omega}\left|\frac{nqs\sigma}{|k|r}-\frac{k^2}{\beta_i^{1/2}qR_0\left(\frac{7}{2}+\frac{2T_e}{T_i}\right)^{1/2}}\right|^{-1}_{r_m^{\rm gap}}. \tag{76}$$

We see that the condition $(\Delta r_{\rm res})_{\rm BAE} > \Delta r_m^{\rm gap}$, needed for the global resonance mechanism being active can never be satisfied, in the considered limits, if $s\sigma < 0$. In this case, indeed,

$$(\Delta r_{\rm res})_{\rm BAE} \lesssim \frac{\gamma}{\omega}\frac{|k|r_m^{\rm gap}}{nq(r_m^{\rm gap})|s|} \ll \Delta r_m^{\rm gap} \tag{77}$$

In the opposite case ($s\sigma > 0$), it could be satisfied only if

$$\frac{k^2}{\beta_i^{1/2}q(r_m^{\rm gap})R_0\left(\frac{7}{2}+\frac{2T_e}{T_i}\right)^{1/2}} \sim \frac{nq(r_m^{\rm gap})|s|}{|k|r_m^{\rm gap}}, \tag{78}$$

but this would imply

$$(\Delta r_{\rm res}^{\rm global})_{\rm BAE} \sim \frac{\gamma}{\omega}\frac{|k|r_m^{\rm gap}}{nq(r_m^{\rm gap})|s|} \ll \Delta r_m^{\rm gap} < \Delta r_m^{\rm harm}. \tag{79}$$

We can conclude that the global resonance mechanism can hardly affect the confinement of resonant ions, as far as we are concerned with a single-(large)-n gap mode, and that the width of the dominant poloidal harmonic constitutes a hard upper bound to the radial displacement of resonant transit fast ions induced by such mode, irrespectively of the existence of a large global mode structure formed by many harmonics. Note that taking into account, in the expression of the resonance frequency, the effect of a finite orbit width of the order of the poloidal harmonic width (Eq. 61), would bring to recognise that the same particle can resonate with more than a single harmonic or couple of harmonics[54]. This is, however, a feature of the basic linear mode-particle interactions, and should not be confused with the global resonance mechanism caused by successive nonlinear radial displacements. Our qualitative conclusion on the largest expected overall fast-ion redistribution then maintains its validity.

VII. SUMMARY AND CONCLUSIONS

In this paper we have investigated the nonlinear dynamics of Alfvén modes driven unstable by fast ions in Tokamaks. Our investigation was focused on gap modes characterised by a single toroidal number. The evolution of such modes is typically characterised by a constant frequency. Under such conditions, it is possible to identify two constant of the perturbed particle motion: the magnetic momentum and a suited combination of toroidal angular momentum and kinetic energy. The existence of these two invariants allows us to cut the phase space into slices orthogonal to the corresponding axes. The dynamics of each slice is not affected by that of other slices; in other words, mode-particle interactions for each slice evolve in an autonomous way, as no particle flux is allowed from one slice to the other. We relied on this feature to examine in detail the behaviour of a significant resonant-particle population; namely, that yielding a peak of the power transfer driving the mode unstable in the linear phase.

We analysed the results of simulations obtained by different numerical codes, related to different modes. In particular, XHMGC simulations of $n = 2$ BAEs were considered, as well as HAGIS simulations of $n = 6$ TAEs. Simulations of the bump-on-tail instability performed by PIC1DP were also considered.

The common aspect presented by all these cases is that mode saturation occurs as the flattening of the resonant-particle distribution function, induced by the fluxes associated to the motion of particles captured in the potential well of the wave, extends over the whole phase-space region where the linear-phase mode-particle power transfer can take place. Two regimes can be distinguished. The first regime is characterised by the fact that such power-transfer region is mainly limited by the need of satisfying the resonance condition $|\omega - \omega_{\rm res}| \lesssim \gamma$. This is the case occurring, *ceteris paribus*, for low values of the growth rate, sharp profiles of the resonance frequency, large mode structures. The second regime, occurring in the opposite limits, sees the power-transfer region limited by the finite width of the mode structure. The two different regimes correspond to different scalings of the saturation mode amplitude with the linear growth rate: the former (*resonance detuning* regime) exhibits a quadratic scaling; the latter (*radial decoupling* regime), a linear scaling.

We have justified these numerical observation on the basis of a simple nonlinear pendulum model. For that model, we have recovered an approximate analytic solution yielding the

instantaneous width of the flattening region in terms of the instantaneous mode amplitude and the linear growth rate. We have shown that such approximate solution correctly predicts the scalings of the saturation amplitude with γ obtained from the full numerical solution of the model, as well as, with a fair agreement, the nonlinear evolution of bump-on-tail instability and Alfvén gap modes.

The fact that the resonant ion redistribution is limited, depending on the saturation regime, by resonance width or mode width allows us to obtain an upper bound for the radial displacement we can expect from the interaction between a single-toroidal-number gap mode and fast ions. We have evaluated such bound for passing ions in the presence of large-n BAEs, TAEs and EAEs, showing that, for low shear, a hard limit is set by the radial width of the quite narrow single poloidal harmonic (of the order of $r_m^{\rm gap}/nq$). If the shear is large enough to allow for the existence of a global mode constituted by several poloidal harmonics, the consequent steepening of the radial profile of the resonance frequency yields an even stricter constraint, further reducing the flattening width by a factor of order γ/ω: there is no chance, for the transit ion, to be displaced for a relevant fraction of the global mode width by successive resonant interactions with different poloidal harmonics. This evaluation could be easily extended to the interaction between gap modes and trapped fast ions.

This paper does not study more complicate situations, which can, however, be important in realistic burning-plasma scenarios. In particular, it does not address the dynamics of Alfvén modes characterised by frequency chirping, the synergic effect of different toroidal mode numbers, the direct mode-mode coupling (not mediated by mode-particle interactions). These aspects will be the subject of future investigations.

VIII. ACKNOWLEDGEMENTS

The authors are indebted to Fulvio Zonca for helpful discussions. This work has been carried out within the framework of the EUROfusion Consortium and has received funding from the Euratom research and training programme 2014-2018 under grant agreement No 633053. The views and opinions expressed herein do not necessarily reflect those of the European Commission. The support from the EUROfusion Researcher Fellowship programme under the task agreement WP14-FRF-IPP/Schneller is gratefully acknowledged.

Some of the simulations for this work were run on the Hydra high performance computer of the Max Planck Society, operated by the MPCDF. For the other simulations, computing resources and the related technical support have been provided by CRESCO/ENEAGRID High Performance Computing infrastructure and its staff.

---

[1] L. Chen and F. Zonca, *Nucl. Fusion* **47**, S727 (2007).

[2] L. Chen and F. Zonca, Phys. Plasmas **20**, 055402 (2013).

[3] Ph. Lauber, Phys. Rep. **533**, 33 (2013).

[4] N. N. Gorelenkov and S. D. Pinches and K. Toi, Nucl. Fusion **54**, 125001 (2014).

[5] S. D. Pinches and I. T. Chapman and Ph. W Lauber and H. J. C Oliver, S. E. Sharapov, K. Shinohara and K. Tani, Phys. Plasmas **22**, 021807 (2015).

[6] L. Chen and F. Zonca, *Rev. Mod. Phys.***88**, 015008 (2016).

[7] L. Chen,Phys. Plasmas **1** 1519 (1994).

[8] H.L. Berk and B.N. Breizman, Phys. Fluids B **2** 2246 (1990).

[9] H. L. Berk, B. Breizman and M. Pekker, Phys. Rev. Lett. **76** 1256, (1996)

[10] H.L. Berk, B.N. Breizman and N.V. Petiashivili, Phys. Lett. A **234** 213 (1997).

[11] T. M. O'Neil, Phys. Fluids **8** 2255 (1965).

[12] T. M. O'Neil and J. H. Malmberg, Phys. Fluids **11** 1754 (1968).

[13] T. M. O'Neil et al., Phys. Fluids **14** 1204 (1971).

[14] T. M. O'Neil and J. H. Winfrey, Phys. Fluids **15** 1514 (1972).

[15] S. Briguglio, F. Zonca and G. Vlad, Phys. Plasmas **5** 3827 (1998).

[16] F. Zonca *et al.*, Nucl. Fusion **45** 477 (2005).

[17] L. Chen and F. Zonca, Phys. Plasmas **20** 055402 (2013).

[18] F. Zonca, L. Chen, S. Briguglio, G. Fogaccia, G. Vlad, and X. Wang, New J. Phys., **17** 013052 (2015).

[19] K. McGuire, et al., Phys. Rev. Lett., **50** 891 (1983).

[20] R. B. White, et al.,Phys. Fluids **26** 2958 (1983).

[21] S. Briguglio *et al.*, Phys. Plasmas **21** 112301 (2014).

[22] M. Schneller, et al., Plasma Physics and Controlled Fusion **58** 014019 (2015).

[23] X. Wang, et al., Structure of wave-particle interactions in nonlinear Alfvnic fluctuation dynamics, 14th IAEA Technical Meeting on Energetic Particles in Magnetic Confinement Systems. Vienna, 2015

[24] X. Wang, S. Briguglio, Ph. Lauber, V. Fusco, and F. Zonca, Phys. Plasmas **23** 012514 (2016).

[25] R. B. WhiteCommun. Nonlinear Sci. Numer. Simulat. **17** 2200 (2012) .

[26] S. Briguglio, G. Vlad, F. Zonca and C. Kar, Phys. Plasmas **2** 3711 (1995).

[27] X. Wang *et al.*, Phys. Plasmas **18** 052504 (2011).

[28] S. D. Pinches,et al., Computer Physics Communications **111** 133 (1998).

[29] W. Deng and G. Fu, Computer Physics Communications, **185** 96 (2014).

[30] http://wdeng.info/codes/pic1dp/.

[31] W. Park, et al., Phys. Fluids B, **4** 2033 (1992).

[32] S. Briguglio, G. Vlad, F. Zonca and G. Fogaccia, Physics Letters A **302** 308 (2002).

[33] F. Zonca, S. Briguglio, L. Chen, S. Dettrick, G. Fogaccia, D. Testa and G. Vlad, Physics of Plasmas **9** 4939 (2002).

[34] S. Briguglio, G. Fogaccia, G. Vlad, F. Zonca, K. Shinohara, M. Ishikawa and M. Takechi, Physics of Plasmas **14** 055904 (2007).

[35] G. Vlad, et al., Nuclear Fusion **49** 075024 (2009)

[36] G. Vlad, S. Briguglio, G. Fogaccia and F. Zonca, Plasma Physics and Controlled Fusion **46** S81 (2004).

[37] G. Vlad, S. Briguglio, G. Fogaccia, F. Zonca and M. Schneider, Nuclear Fusion **46** 1 (2006).

[38] A. Cardinali, et al., Energetic particle physics in FAST H-mode scenario with combined NNBI and ICRH, in Fusion Energy 2010, IAEA, Vienna, 2010, Paper THW/P7-04

[39] C. Di Troia, S. Briguglio, G. Fogaccia, G. Vlad and F. Zonca, Simulation of EPM dynamics in FAST plasmas heated by ICRH and NNBI, in 24th IAEA FEC 2012, San Diego 8-13 Oct. 2012, paper TH/P6-21

[40] A. Pizzuto, et al., Nuclear Fusion **50**, 095005 (2010).

[41] R. Izzo, et al., Phys. Fluids **26** 2240 (1983).

[42] F. Zonca and L. Chen, Phys. Plasmas **21**, 072120 (2014).

[43] F. Zonca and L. Chen, Phys. Plasmas **21**, 072121 (2014).

[44] Ph. Lauber, et al., Journal of Computational Physics **226** 447 (2007).

[45] S. D. Pinches, et al., Plasma Phys. Control. Fusion **46** S47 (2004).

[46] M. Schneller, et al., Nuclear Fusion **53** 123003 (2013).

[47] http://phoenix.ps.uci.edu/zlin/pic1d/.

[48] http://www.mcs.anl.gov/petsc/.

[49] L. Chen and F. Zonca, *Rev. Mod. Phys.* **88** 015008 (2016).

[50] F. Zonca, S. Briguglio, L. Chen, G. Fogaccia, G. Vlad and X. Wang, "Nonlinear dynamics of phase-space zonal structures and energetic particle physics", Proceedings of the 6th IAEA Technical Meeting on "Theory of Plasma Instabilities"', Vienna, Austria, May 27-29 (2013).

[51] A. Mishchenko, A. Könies, R. Hatzky, *Phys. Plasmas* **16** 082105 (2009).

[52] A. Könies et al., "Benchmark of gyrokinetic, kinetic MHD and gyrofluid codes for the linear calculation of fast particle driven TAE dynamics", Proceedings of the 24th IAEA Fusion Energy Conference, San Diego, USA, Oct. (2012).

[53] M. Abramowitz and I.A. Stegun. Handbook of Mathematical Functions. Dover, 1972.

[54] A. Bierwage and K. Shinohara, *Phys. Plasmas* **21** 112116 (2014).